Abstract

Xudong Xiao: Large-Eddy Simulation/Reynolds-Averaged Navier-Stokes Hybrid Schemes for High Speed Flows. (Under the direction of Dr. H. A. Hassan)

Three LES/RANS hybrid schemes have been proposed for the prediction of high speed separated flows. Each method couples the k–ζ(Enstrophy) RANS model with an LES subgrid scale one-equation model by using a blending function that is coordinate system independent. Two of these functions are based on turbulence dissipation length scale and grid size, while the third one has no explicit dependence on the grid. To implement the LES/RANS hybrid schemes, a new rescaling-reintroducing method is used to generate time-dependent turbulent inflow conditions. The hybrid schemes have been tested on a Mach 2.88 flow over 25 degree compression-expansion ramp and a Mach 2.79 flow over 20 degree compression ramp. A special computation procedure has been designed to prevent the separation zone from expanding upstream to the recycle-plane. The code is parallelized using Message Passing Interface (MPI) and is optimized for running on IBM-SP3 parallel machine.

The scheme was validated first for a flat plate. It was shown that the blending function has to be monotonic to prevent the RANS region from appearing in the LES region. In the 25 deg ramp case, the hybrid schemes provided better agreement with experiment in the

recovery region. Grid refinement studies demonstrated the importance of using a grid independent blend function and further improvement with experiment in the recovery region. In the 20 deg ramp case, with a relatively finer grid, the hybrid scheme characterized by grid independent blending function well predicted the flow field in both the separation region and the recovery region. Therefore, with “appropriately” fine grid, current hybrid schemes are promising for the simulation of shock wave/boundary layer interaction problems.

LARGE-EDDY SIMULATION / REYNOLDS-AVERAGED NAVIER-STOKES HYBRID SCHEMES FOR HIGH SPEED FLOWS

by

Xudong Xiao

A dissertation submitted to the graduate faculty of
North Carolina State University
in partial fulfillment of the
requirements for the Degree of
Doctor of Philosophy

Department of Mechanical and Aerospace Engineering

Raleigh
October 2002

Approved By:

Dr. F. R. DeJarnette	Dr. J. R. Edwards
Dr. R. E. Funderlic	Dr. D. S. McRae

Dr. H. A. Hassan, Chair

Biography

Xudong Xiao was born on September 22, 1972 to Dai and Gongmiao Xiao in Sanming, Fujian, P. R. China. His birthday happened to be the Moon Festival(Mid-Autumn) in Chinese lunar calendar. Xudong spent his first 18 years in this small town in the southeast of China. Following his sister's foot-print, he attended Sanming Shiyan Elementary School, Sanming No.1 Middle/High school. In the summer of 1990, with his dream and the encouragement from his family, he left his hometown and started his collegiate life in Nanjing University of Aeronautics and Astronautics(NUAA), where he majored in Aeroengine Design. After he earned the bachelor degree in 1994, he and his girlfriend, Yanglin Yu, who became his wife 3 years later, continued their study in NUAA for their master degrees.

In April 1997, he got his master degree and moved to Guangzhou, Guangdong (Canton), where he worked for Southern and Central Regional Administration of Civil Aviation Administration of China(CAAC). In December 1997, he married Yanglin Yu.

In 1999, he went to North Carolina State University to pursue his Ph.D degree under the direction of Dr. H. A. Hassan. When writing this dissertation, he and his wife are expecting their first baby.

Acknowledgments

First and foremost, I feel indebted to my advisor, Dr. H. A. Hassan, not only for the opportunity he gave me to study in NCSU, the years of guidance and help he provided me in various area, but also for the influence I got from his personality and, the most memorable, his diligence. Special thanks go to Dr. J. R. Edwards for providing me with the code and discussing various implementation issues. I would also like to thank Dr. D. S. McRae for his help in my CFD course work and research. Thanks also go to Dr. R. E. Funderlic for serving on my advisory committee. I am also thankful to Dr. N. Chokani for being willing but unable to attend my final oral exam as a committee member due to his sabbatical, and Dr. F. R. DeJarnette for agreeing to serve as a committee member on short notice.

Also I am grateful to my wife, Yanglin Yu, for her understanding, and companying me for so many years. Without her “pushing”, I may not have reached this stage.

I would like to acknowledge North Carolina Super Computing Center for granting computer time and the service provided by Dr. Mark Reed and his colleagues. Thanks also go to NCSU for supporting my study.

At this moment, I would like to thank Ryan Bond and Ryan McDaniel for helping me adjust to new environments after I came to this country, and all my former and current officemates in Langley room for their friendliness and help.

Table of Contents

List of Tables

List of Figures

List of Symbols

$\mathbf{A}$, $\mathbf{B}$, $\mathbf{C}$, $\mathbf{D}$	Flux Jacobian matrices
C_p	Specific heat at constant pressure
C_v	Specific hear at constant volume
E	Total energy per unit mass
$\mathbf{F}$, $\mathbf{G}$, $\mathbf{H}$	Flux vectors
H	Total enthalpy per unit mass
J	Jacobian of coordinate transformation
k	Subgrid turbulence kinetic energy or Fluctuation kinetic energy per unit mass,
l_ϵ	Dissipation length scale
l_s	von Karman length scale
M	Mach number
p	Pressure
Pr	Laminar Prandtl number
Pr_t	Turbulent Prandtl number
Q_i	Subgrid scale turbulence heat flux vector, or Reynolds heat flux vector
q_i	Laminar heat flux vector
R	Gas constant
$\mathbf{S}$	Source term
S_{ij}	Strain-rate tensor
t	Time
T	Temperature
$\mathcal{T}_{ij}$	Stress tensor
U	Time-averaged velocity
$\mathbf{U}$	Vector of conservative variables
$\mathcal{U}$, $\mathcal{V}$, $\mathcal{W}$	Contravariant velocity component
u, v, w	Velocity component in x, y, z direction, respectively
u_i	Velocity vector
V	Grid cell volume
$\mathbf{W}$	Vector of primitive variables
x, y, z	Coordinate directions in physical space
x_i	Position vector
α_1	Model constant in blending functions
Γ, Γ_1, Γ_2, Γ_3	Blending functions
Δ_m, Δ_v	Grid cell size
δ	Boundary layer thickness

δ_{ij}	Kronecker delta
ξ, η, ς	Coordinate directions in computational space
ζ	Enstrophy
θ	Boundary layer momentum thickness
λ	Taylor's microscale
μ	Laminar(molecular) viscosity coefficient
μ_t	Turbulent(eddy) viscosity coefficient
ν	Kinematic laminar(molecular) viscosity coefficient
ν_t	Kinematic turbulent(eddy) viscosity coefficient
ρ	Density
σ_{ij}	Deviatoric part of strain-rate tensor
τ_{ij}	Subgrid scale stress tensor, or Reynolds stress tensor
Ω_i	Vorticity vector
Ω	Magnitude of vorticity, $\sqrt{\Omega_i \Omega_i}$

Subscripts:

∞	Denotes freestream quantity
e	Denotes boundary layer edge quantity
eff	Denotes effective quantities
i, j, k	Denotes spatial coordinates or cell indices
$inlet$	Denotes inlet quantities
$recy$	Denotes recycle-plane quantities
t	Denotes turbulent quantities
w	Denotes wall quantities

Superscript:

$'$	Denotes subgrid scale component, or time-averaged fluctuating component
$''$	Denotes Favre-averaged fluctuating components
inn	Denotes boundary layer inner region
out	Denotes boundary layer outer region

Accents:

$\bar{}$	Denotes spatially filtered quantities
$\tilde{}$	Denotes Favre-filtered quantities
$\hat{}$	Denotes time-averaged quantities
$\check{}$	Denotes Favre-averaged quantities

Abbreviations:

CFD	Computational Fluid Dynamics
DES	Detached-Eddy Simulation
DNS	Direct Numerical Simulation

LES	Large Eddy Simulation
RANS	Reynolds-averaged Navier-Stokes equations
RMS	Root Mean Square
SGS	Subgrid Scale
TLM	Two-Layer Models
VLES	Very Large-Eddy Simulation

Chapter 1

Introduction

Because of its frequent occurrence in engineering applications, turbulence has been the subject of study for a long time. It is characterized by a three-dimensional, time-dependent, and random flow field, where a large range of time scales and length scales exists. Although it can be described by the Navier-Stokes equations, the analytical solution to turbulent flow is not possible. Thus, Computational Fluid Dynamics(CFD) becomes a powerful tool to predict turbulent flows. In general, there are three kinds of approaches for turbulence simulation:

1. Direct Numerical Simulation(DNS);
2. Large-Eddy Simulation(LES);
3. Reynolds-Averaged Navier-Stokes(RANS).

In DNS, the Navier-Stokes equations are solved to determine the instantaneous flow field. All length scales and time scales must be resolved. Hence, no modeling is needed. Since the ratio of the largest length scale, L, to the smallest, Kolmogorov length scale, η, is of the order of $Re^{\frac{3}{4}}$, and the smallest grid size must be of order η, the number of grid nodes for a three dimensional turbulence flow will be of the order $Re^{\frac{9}{4}}$. Moreover, relative to the largest time scale, the smallest time scale decreases as $Re^{-\frac{3}{4}}$. Hence, the overall cost of

DNS is of order Re^3[1], which is computationally expensive. As a result, DNS is restricted to flows with low-to-moderate Reynolds number, and thus is considered as a research tool for turbulence [2], and not a general solver for engineering problems.

In the other extreme, RANS approaches model all scales and solve time-averaged equations. The resulting flow field is represented by the mean properties. Additional model equations are solved for Reynolds stresses. If a turbulence viscosity model is used, the turbulence viscosity, or eddy viscosity, can be obtained explicitly from an algebraic relation, or implicitly by solving some partial differential equations of turbulence quantities, like k–ω, k–ϵ and k–ζ models. The Reynolds stresses can then be determined from the Boussinesq assumption. In RANS approaches, the cost does not significantly increase with Reynolds number, since all scales of turbulent motion are modeled. Because of its efficiency, RANS approaches are dominant in current CFD applications. Various RANS models are now available for different flows. But for the shock-induced boundary layer separations, "*far less improvement has been made with turbulence models for such flows*"([3], page 261).

For LES, the spatially-filtered Navier-Stokes equations are solved. The large scales of three-dimensional unsteady turbulent motion can be calculated directly, but the eddies smaller than the grid size have to be modeled (subgrid scale(SGS) modeling). Since, experimentally and theoretically, the energy-dissipating eddies (small eddies) can be considered universal, the uncertainty of SGS modeling should be less than that of RANS. So LES is believed to be more accurate than RANS, especially for separated flows[1]. For wall-bounded flows, LES grid requirement in the outer region of boundary layer is proportional to $Re^{0.4}$, while in the inner layer, in order to resolve viscous sublayer streaks, the number

of grid points is proportional to $Re^{1.8}$(Chapman[4]). So the cost of LES with near-wall resolution is between DNS and RANS. However, LES is still prohibitively expensive for high speed flows.

Motivated by the limitations of LES and RANS, endeavors have been devoted in past decades toward reducing the grid resolution requirements at the near-wall region for LES. When the grid in the inner layer is too coarse, the effect of the wall layer must be modeled[5]. Depending on the complexity of inner layer modeling, three major types of modeling techniques have been developed, as shown in Figure 1.1.

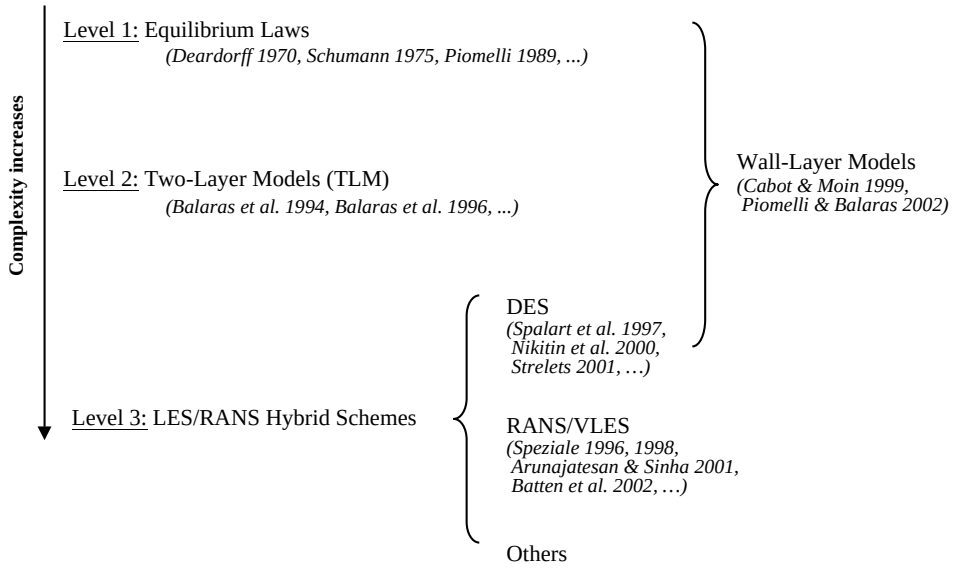

Figure 1.1: LES with inner layer modeling.

Most of the equilibrium laws compute the wall stress by using log law of the wall at some distance away from the wall. Some examples can be found in Deardorff[6],

Schumann[7], Piomelli[8], *etc*. As is known, the law of the wall is not valid for separated flows. So it is difficult to extend this approach to more complex turbulent flows.

Rather than using simple relations from the law of the wall, two-layer models(TLM) solve a simplified set of differential equations(i.e., boundary layer equations) in the near wall region. This method was proposed by Balaras & Bennocci[9] and Balaras *et al.*[10]. In this approach, the boundary layer equations are solved on a fine grid embedded in the coarser LES grid. The exchange of boundary conditions between the two grids is somewhat like that used in Chimera scheme[11]: the coarse LES grid provides free stream conditions for inner layer simulation, and the wall stress calculated in the embedded mesh returns to the coarse LES mesh as a wall boundary condition. Note that two grids and two sets of equations are involved.

In the third level, the LES/RANS hybrid schemes use one grid (at least in the wall normal direction) and solve a more complete set of equations – the RANS equations in the near-wall region. Different turbulence models are applied to different regions. In the vicinity of the wall, the RANS model is used, whereas, away from the wall, the eddy-viscosity is calculated from LES SGS model.

Up till now, there are two major techniques among LES/RANS hybrid schemes. One is the "Detached-Eddy Simulation", advocated by Spalart *et al.*[12] for the simulation of massively separated flows. In [5], DES, TLM and equilibrium laws models are considered as "Wall-Layer Models". Recent reviews of wall-layer models can be found in Cabot & Moin[13] and Piomelli & Balaras[5].

In DES, the distance to the nearest wall, d, in the Spalart-Allmaras one-equation model[14] destruction term is replaced with a new length scale $\tilde{d}$:

$$\tilde{d} = \min(d, C_{DES}\Delta) \tag{1.1}$$

where C_{DES} is a model constant, and Δ the largest mesh spacing in all directions:

$$\Delta = \max(\Delta_x, \Delta_y, \Delta_z) \tag{1.2}$$

In the near wall region, $\tilde{d} = d$, the modified S-A model functions as the original model. When it is far away from the wall, $\tilde{d} = C_{DES}\Delta$, and the model equation works as an SGS stress model for LES. In this "LES region", when the production and the destruction of S-A model are balanced, it produces the eddy viscosity $\nu_t \propto S\Delta^2$ [12], which is similar to Smagorinsky SGS model[15].

In standard DES, the entire incoming boundary layer is simulated with RANS by using a so-called "RANS grid", where the mesh spacing parallel to the wall is so large that $\tilde{d} = d$ in the entire boundary layer. While in the separated regions , the mesh is refined in all direction, then LES can be used. More mesh issues for DES can be found in [16]. But in Nikitin *et al.*[17], DES approach is applied to the attached boundary layer in a plane channel flow, where the RANS model in the inner layer is combined with LES at the outer region of the boundary layer. With this approach, they reproduced the logarithmic profiles. However, a so-called "DES buffer layer" or "grey region" showed up and resulted in the logarithmic layer with a high intercept, and, in some cases, incorrect slope, in LES region.

Since the pioneering paper of Spalart *et al.*[12], DES has been applied to various flows, e.g., Travin *et al.*[18], Squires *et al.*[19]. After noticing that S-A model is not superior

to some more sophisticated models, and thus the DES with S-A model might fail in some cases, Strelets[20] extended the DES concept on a two-equation model, i.e., Menter's shear-stress transport(M-SST) model. And instead of the wall distance, the dissipation length scale, $\sqrt{k}/(\beta^*\omega)$, is used as a working parameter. A similar extension was developed by Bush & Mani[21]. Encouraging results have been obtained from their researches.

The other type of LES/RANS hybrid scheme was proposed by Speziale[22; 23], who realized the shortcomings of existing LES SGS models and tried to bridge the gap between DNS, LES and RANS. In his model, the turbulent stress was expressed as a product of Reynolds stress and a damping function:

$$\tau_{ij} = \left[1 - \exp(-\beta\Delta/L_K)\right]^n \tau_{ij}^{(R)} \tag{1.3}$$

where L_K is the Kolmogorov length scale, Δ the grid size, $\tau_{ij}^{(R)}$ the Reynolds stress, and β and n are the model constants. With this damping function, RANS stress models can be recovered in coarse grid, and LES can change to RANS computation smoothly. Similar formula appeared in Arunajatesan and his co-workers[24; 25], and Zhang *et al.*[26]. And recently, the LNS approach of Batten *et al.*[27; 28] used an alternative to the damping function, which they called "latency factor", α,

$$\alpha = \min\left[L \cdot V_{LES}, L \cdot V_{RANS}\right] / L \cdot V_{RANS} \tag{1.4}$$

where L and V are length scale and velocity scale, respectively. In [28], the $L \cdot V_{LES}$ was the kinematic eddy viscosity from Smagorinsky SGS model[15], $C_S(L^\Delta)^2 S^*$, where the L^Δ is the mesh spacing. And the $L \cdot V_{RANS}$ is the kinematic eddy viscosity from a k–ϵ model.

Note that aforementioned hybrid schemes compare different length scales, and decide therefrom the LES or the RANS model to be used in a certain region. In most cases, the grid size is one of the length scale to be compared with. Therefore the "RANS region" and the "LES region" are grid-dependent. It is the user's task to choose different models to operate in different regions. An alternative to these length scale-type approaches is to treat these two regions in a pre-determined manner [29; 30]. Fan and co-workers [31; 32; 33] developed the "flow-dependent" blending function to couple the two-equation RANS model with the LES SGS one-equation model. The working parameters of their blending function are the wall distance and some quantities from model equations, rather than the local grid spacing. Thus, users needn't worry about grid issues.

For the hybrid schemes, one of the problems yet to be solved is the inflow boundary conditions. Because of the LES component, the resulting flow field solved by LES/RANS hybrid schemes has to be three-dimensional and time-dependent. Thus, the inflow boundary condition must be time-dependent. Therefore, as is the case in LES, specification of *turbulent* inflow conditions is also a challenge to LES/RANS hybrid schemes.

Generally, there are two approaches for simulating the turbulent inflow conditions. One is based on random fluctuations ([34], [35], [36], *etc*). The instantaneous velocity field in the inflow boundary is generated by

$$u_i(y,z,t) = U_i(y) + L_{ij}\phi_j(y,z,t) \tag{1.5}$$

where U_i is the mean velocity, L_{ij} defines a lower triangle matrix such that

$$R = LL^T \tag{1.6}$$

$$R_{ij} = \overline{u_i'' u_j''} \tag{1.7}$$

and ϕ_j are three random variates, each of which has zero mean, unit variance and zero covariance with other two variates. L can be calculated using Cholesy factorization. Using this procedure, the random fluctuations can statistically recover the turbulent stresses. In the procedure of Le and Moin[37; 38], the spectrum of fluctuation is defined in Fourier space and the velocity fluctuation distribution is provided by an inverse Fourier transformation. Because the random field is not governed by Navier-Stokes equations, it is not physical and needs a lengthy development section[34]. As was shown in [32] by Fan *et al.*, this approach did not give good results for shock wave / boundary layer interaction problems.

Recently, Batten *et al.*[28] "synthesized" the turbulence: the velocity fluctuations in the overall flow field are generated from stochastic PDEs, which required three additional equations to be solved. This may increase the overhead of computation and suffer from the same difficulty as the other random fluctuation methods.

The other is the so-called rescaling-reintroducing method, which is used to simulate the inflow turbulence over a flat plate. It utilizes the similarities in the turbulent boundary layer, rescales the flow field at a downstream location and then reintroduces the results to the inflow boundary. This method was originally developed by Spalart and Leonard[39], then modified by Lund *et al.*[34]. Recently, it has been extended to compressible supersonic flow by Urbin & Knight[40]. As shown in [34], it is more efficient than the methods based

on random fluctuations. However, in [34] and [40], this approach was only applied to LES. Furthermore, only constant-coefficient SGS model was used. Therefore, this method can not be directly applied to LES/RANS hybrid schemes in which some model equations have to be accounted for.

In this study, three LES/RANS hybrid schemes have been proposed and applied to wall-bounded flows. In these schemes, the k–ζ RANS model is coupled with one-equation subgrid scale LES model through blending functions. Both models and blending functions have no dependence on the wall-distance. Two of the blending functions use grid size as a working parameter. The third one is independent of the local grid spacing. Potentially, these schemes are highly suited for flows characterized by a complex geometry. And based on rescaling-reintroducing method, a method for generating inflow boundary conditions for hybrid schemes has been implemented and validated. All the hybrid schemes have been tested on supersonic compression ramp problems, since the shock wave/boundary layer interaction has been a challenging problem for CFD.

The governing equations will be developed in Chapter 2. Chapter 3 presents the turbulence closure method. The method for generating turbulent inflow boundary conditions is discussed in Chapter 4. In Chapter 5, the configurations for testing hybrid schemes are presented. This chapter also gives the special computation procedure for the application of hybrid schemes to ramp problems. In Chapter 6, the results from different cases are presented and discussed. Chapter 7 gives the concluding remarks.

Chapter 2

Governing Equations

In this chapter, the derivation of governing equations for LES and RANS is presented. As will be shown, the two sets of governing equations have similar form. This feature facilitates the coupling of LES and RANS such that the coupling can be done through turbulence models.

2.1 Navier-Stokes Equations

The governing equations for the conservation of mass, momentum and energy in compressible turbulent flows are:

$$\frac{\partial \rho}{\partial t} + \frac{\partial \rho u_j}{\partial x_j} = 0 \tag{2.1}$$

$$\frac{\partial \rho u_i}{\partial t} + \frac{\partial \rho u_i u_j}{\partial x_j} = -\frac{\partial p}{\partial x_i} + \frac{\partial \mathcal{T}_{ij}}{\partial x_j} \tag{2.2}$$

$$\frac{\partial \rho E}{\partial t} + \frac{\partial \rho H u_i}{\partial x_i} = \frac{\partial}{\partial x_i}\left(\mathcal{T}_{ij} u_j - q_i\right) \tag{2.3}$$

where u_i is the velocity, p the pressure, ρ the density of the fluid, E the total energy per unit mass, H the total enthalpy per unit mass , $\mathcal{T}_{ij}$ the stress tensor, and q_j the heat flux.

E, H and q_i are defined as

$$E = C_v T + \frac{1}{2}\rho u_i u_i \tag{2.4}$$

$$H = C_p T + \frac{1}{2}\rho u_i u_i \tag{2.5}$$

$$q_i = -\frac{\mu C_p}{Pr}\frac{\partial T}{\partial x_i} \tag{2.6}$$

where T is the temperature. In current work, the fluid is assumed to be calorically perfect gas. C_v and C_p are therefore constants.

For Newtonian flows, $\mathcal{T}_{ij}$ are defined as,

$$\mathcal{T}_{ij} = \mu\sigma_{ij}, \tag{2.7}$$

with

$$\sigma_{ij} = 2S_{ij} - \frac{2}{3}\delta_{ij}S_{kk} \tag{2.8}$$

where S_{ij} is the strain-rate tensor,

$$S_{ij} = \frac{1}{2}\left(\frac{\partial u_i}{\partial x_j} + \frac{\partial u_j}{\partial x_i}\right) \tag{2.9}$$

σ_{ij} is the deviatoric part of the strain-rate tensor, μ is the dynamic viscosity which can be determined as a function of temperature using Sutherland's law.

The equation of state $p = \rho RT$ and the assumption of constant Prandtl number Pr close the system.

But in LES and RANS, Equation(2.1)–(2.3) are not the equations that are solved by CFD codes. Instead, the filtered Navier-Stokes equations and Reynolds-Averaged Navier-Stokes equations are solved in LES and RANS simulation, respectively.

2.2 Filtering Operation

To get LES governing equations, a *filtering* operation[1] is defined to decompose the instantaneous quantity into the sum of a filtered component and a residual component,

$$f(\mathbf{r},t) = \overline{f}(\mathbf{r},t) + f'(\mathbf{r},t) \tag{2.10}$$

The general filtering operation on any flow variable f is defined as

$$\overline{f}(\mathbf{x},t) = \int G(\mathbf{r},\mathbf{x}) f(\mathbf{x}-\mathbf{r},t) d\mathbf{r}, \tag{2.11}$$

where the integration is over the whole flow domain, G is a filter function, and $\overline{f}$ is the filtered variable. The filter G is chosen so as to eliminate the fluctuations whose length scales are smaller than the mesh size[41; 42] so that $\bar{f}$ represents the large scales of motion.

Some properties of the filtering operation[1; 23] are summarized as follows:

1. Normalization condition of G. The filter function satisfies

$$\int G(\mathbf{r},\mathbf{x}) d\mathbf{r} = 1 \tag{2.12}$$

2. The operations of filtering and differentiating w.r.t. time commute, i.e.

$$\frac{\partial \overline{f}}{\partial t} = \overline{\frac{\partial f}{\partial t}} \tag{2.13}$$

3. For homogeneous filters, $\frac{\partial G(\mathbf{r},\mathbf{x})}{\partial x_j} = 0$, the operations of filtering and differentiating w.r.t. position commute, i.e.

$$\frac{\partial \overline{f}}{\partial x_j} = \overline{\frac{\partial f}{\partial x_j}} \tag{2.14}$$

Most commonly-used filtered functions are homogeneous. Some examples can be found in [1], pp. 563.

4. Different from Reynolds averages,

$$\overline{\overline{f}} \neq \overline{f}, \qquad \overline{f'} \neq 0 \tag{2.15}$$

5. $\overline{f}$ depends on time. Therefore, an LES must be a time-dependent computation.

In order to eliminate terms that require modeling in the continuity equation, Favre-averaging[43] is introduced:

$$\tilde{f} \equiv \frac{\overline{\rho f}}{\overline{\rho}} \tag{2.16}$$

2.3 Filtered Compressible Navier-Stokes Equations

The filtering of Equation(2.1)–(2.3) can be expressed in the conservation form[44]:

$$\frac{\partial \bar{\rho}}{\partial t} + \frac{\partial}{\partial x_j}\left(\bar{\rho}\tilde{u}_j\right) = 0 \tag{2.17}$$

$$\frac{\partial}{\partial t}\left(\bar{\rho}\tilde{u}_i\right) + \frac{\partial}{\partial x_j}\left(\bar{\rho}\tilde{u}_i\tilde{u}_j\right) = -\frac{\partial \bar{p}}{\partial x_i} + \frac{\partial}{\partial x_j}\left(\tilde{\mathcal{T}}_{ij} + \tau_{ij}^{SGS}\right) \tag{2.18}$$

$$\frac{\partial}{\partial t}\left(\bar{\rho}\tilde{E}\right) + \frac{\partial}{\partial x_j}\left(\bar{\rho}\tilde{H}\tilde{u}_j\right) = \frac{\partial}{\partial x_j}\left(\tilde{u}_i(\tilde{\mathcal{T}}_{ij} + \tau_{ij}^{SGS}) - (\tilde{q}_j + Q_j^{SGS})\right) \tag{2.19}$$

where $\bar{\rho}$ is filtered density, $\tilde{u}_i$ are the components of Favre-filtered velocity, $\bar{p} = \bar{\rho}R\tilde{T}$ is the filtered pressure, $\tilde{E}$ and $\tilde{H}$ are the filtered total energy and total enthalpy per mass, respectively,

$$\bar{\rho}\tilde{E} = \bar{\rho}C_v\tilde{T} + \frac{1}{2}\bar{\rho}\tilde{u}_i\tilde{u}_i + \bar{\rho}k \tag{2.20}$$

$$\bar{\rho}\tilde{H} = \bar{\rho}C_p\tilde{T} + \frac{1}{2}\bar{\rho}\tilde{u}_i\tilde{u}_i + \bar{\rho}k \tag{2.21}$$

where k is subgrid scale turbulence kinetic energy per mass

$$k \equiv \frac{1}{2}\left(\widetilde{u_i u_j} - \tilde{u}_i\tilde{u}_j\right) \tag{2.22}$$

The filtered stress $\tilde{\mathcal{T}}_{ij}$ is defined as

$$\tilde{\mathcal{T}}_{ij} \equiv \mu(\tilde{T})\tilde{\sigma}_{ij} \tag{2.23}$$

where

$$\tilde{\sigma}_{ij} = \frac{\partial \tilde{u}_i}{\partial x_j} + \frac{\partial \tilde{u}_j}{\partial x_i} - \frac{2}{3}\delta_{ij}\frac{\partial \tilde{u}_k}{\partial x_k} \tag{2.24}$$

The subgrid scale stress, τ_{ij}^{SGS}, is defined as

$$\tau_{ij}^{SGS} \equiv -\bar{\rho}(\widetilde{u_i u_j} - \tilde{u}_i\tilde{u}_j) \tag{2.25}$$

The filtered heat flux, $\tilde{q}_j$, is defined as

$$\tilde{q}_j \equiv \frac{\mu(\tilde{T})C_p}{Pr}\frac{\partial \tilde{T}}{\partial x_j} \tag{2.26}$$

The subgrid scale turbulence heat flux, Q_j^{SGS}, is defined as

$$Q_j^{SGS} \equiv \bar{\rho}(\widetilde{Tu_j} - \tilde{T}\tilde{u}_j) \tag{2.27}$$

To get Equations (2.17)–(2.19), it is assumed that[44]

$$\tilde{\mathcal{T}}_{ij} \approx \overline{\mu\sigma_{ij}} \tag{2.28}$$

$$\tilde{q}_j \approx \overline{\frac{\mu(T)C_p}{Pr}\frac{\partial T}{\partial x_j}} \tag{2.29}$$

$$\tilde{\mathcal{T}}_{ij}\tilde{u}_i \approx \overline{\mathcal{T}_{ij}u_i} \tag{2.30}$$

$$\tau_{ij}^{SGS}\tilde{u}_i \approx -\frac{1}{2}\bar{\rho}(\widetilde{u_i u_i u_j} - \tilde{u}_i\tilde{u}_i\tilde{u}_j - 2k\tilde{u}_j) \tag{2.31}$$

The subgrid scale stresses τ_{ij}^{SGS} and heat flux Q_j^{SGS} can not be computed directly and thus have to be modeled. When an eddy viscosity SGS model is employed, these two terms

can be modeled as

$$\tau_{ij}^{SGS} = \mu_t \tilde{\sigma}_{ij} + \frac{2}{3}\bar{\rho}k\delta_{ij} \tag{2.32}$$

$$Q_j^{SGS} = -\frac{\mu_t C_p}{Pr_t}\frac{\partial \tilde{T}}{\partial x_j} \tag{2.33}$$

where μ_t is the eddy viscosity for LES and $Pr_t \approx 0.89$ is considered as a constant for turbulent flows.

2.4 Reynolds-Averaged Navier-Stokes(RANS) Equations

The governing equations can be further simplified by using Reynolds averaging [45]. The resulting equation is so-called RANS. In this approach, the flow property can be decomposed into mean and fluctuating components

$$f = \hat{f} + f' \tag{2.34}$$

where f denotes any flow properties, f' is the fluctuation around $\hat{f}$ or the time-averaged value of f, which is defined as

$$\hat{f} = \frac{1}{\tau}\int_{t_0}^{t_0+\tau} f(\mathbf{x}, t)dt \tag{2.35}$$

where τ is a period of time that is much longer than the time-scale of turbulent fluctuations.

The Favre-average for time-averaging is defined as

$$\check{f} = \frac{\widehat{\rho f}}{\hat{\rho}} \tag{2.36}$$

Therefore, the decomposition of f can then be rewritten as

$$f = \check{f} + f'' \tag{2.37}$$

where f'' is the fluctuations imposed on $\check{f}$.

Apply the Reynolds averaging procedure to the original Navier-Stokes equations, we can obtain the RANS equations (c.f.[3] for detailed derivation):

$$\frac{\partial \hat{\rho}}{\partial t} + \frac{\partial}{\partial x_j}\left(\hat{\rho}\check{u}_j\right) = 0 \tag{2.38}$$

$$\frac{\partial}{\partial t}\left(\hat{\rho}\check{u}_i\right) + \frac{\partial}{\partial x_j}\left(\hat{\rho}\check{u}_i\check{u}_j\right) = -\frac{\partial \hat{p}}{\partial x_i} + \frac{\partial}{\partial x_j}\left(\hat{\mathcal{T}}_{ij} + \tau_{ij}^{RANS}\right) \tag{2.39}$$

$$\frac{\partial}{\partial t}\left(\hat{\rho}\check{E}\right) + \frac{\partial}{\partial x_j}\left(\hat{\rho}\check{H}\check{u}_j\right) = \frac{\partial}{\partial x_j}\left(\check{u}_i\left(\hat{\mathcal{T}}_{ij} + \tau_{ij}^{RANS}\right) - \left(\hat{q}_j + Q_j^{RANS}\right)\right) \tag{2.40}$$

In Equations(2.38)-(2.40),

$$\tau_{ij}^{RANS} \equiv -\hat{\rho}\widehat{u_i'' u_j''} \tag{2.41}$$

$$Q_j^{RANS} \equiv \widehat{\rho u_j'' h''} \tag{2.42}$$

$$\hat{\rho}k \equiv \frac{1}{2}\widehat{\rho u_i'' u_i''} \tag{2.43}$$

where τ_{ij}^{RANS} is Reynolds-stress tensor, Q_j^{RANS} denotes turbulent heat-flux vector, and k is the turbulence kinetic energy, $\check{E}$ and $\check{H}$ are averaged total energy and total enthalpy per unit mass, respectively.

Using Boussinesq approximation, and denoting the eddy viscosity by μ_t, the resulting expression for the modeled Reynolds-stresses has the same form as Equation(2.32). μ_t can be obtained from model equations, such as k–ω, k–ζ models, *etc*. The RANS and the model equations close the system.

Note that the governing equations for the RANS [Eqs. (2.38) – (2.39)] and the LES [Eqs.(2.17) – (2.19)] have similar form. Therefore, both sets of equations can be solved with a single numerical scheme.

Chapter 3

LES/RANS Coupling

The governing equations of LES and RANS have the same form. There is no coupling issue in the governing equations. The coupling of LES and RANS relies on how the eddy-viscosity is calculated. In this study, it is implemented by "blending" one-equation LES SGS turbulence model with two-equation k–ζ model through a *blending function*, which makes the turbulence model change smoothly from a RANS model in the near-wall region to an LES SGS model far away from the wall.

3.1 Hybrid Turbulence Model

The hybrid LES/RANS turbulence modeling consists of two sets of model equations. One is the k–ζ two-equation model[46] for the RANS component. The other is the one-equation SGS model for the LES part.

k–ζ model has been successfully applied to different turbulent flows, including free shear flows and wall-bounded shear flows, in both low speed and high speed cases[46; 47; 48]. Its transitional extension predicts well the onset and extent of transition in two and three dimensional transitional flows[49; 50]. Because it is free of wall and damping functions, it is a good candidate for the implementation of a hybrid scheme that has no

explicit dependence on the geometry.

The k and ζ equations in the k–ζ model are defined as[46]:

$$\begin{aligned}
\frac{\partial \overline{\rho} k}{\partial t} + \frac{\partial \overline{\rho} \tilde{u}_j k}{\partial x_j} &= \frac{\partial}{\partial x_j}\left[\left(\frac{\mu}{3} + \frac{\mu_t}{\sigma_k}\right)\frac{\partial k}{\partial x_j}\right] \\
&\quad + \tau_{ij}\frac{\partial \tilde{u}_i}{\partial x_j} - \frac{1}{C_k}\frac{\mu_t}{\overline{\rho}^2}\frac{\partial \overline{\rho}}{\partial x_i}\frac{\partial \overline{P}}{\partial x_i} - C_1\frac{\overline{\rho} k}{\tau_\rho} - \mu\zeta \qquad (3.1) \\
\frac{\partial \overline{\rho} \zeta}{\partial t} + \frac{\partial \overline{\rho} \tilde{u}_j \zeta}{\partial x_j} &= \frac{\partial}{\partial x_j}\left[\left(\mu + \frac{\mu_t}{\sigma_\zeta}\right)\frac{\partial \zeta}{\partial x_j}\right] + \frac{\mu_t}{\sigma_r}\frac{\partial \Omega_i}{\partial x_j}\left(\frac{\partial \Omega_i}{\partial x_j} + \frac{\partial \Omega_j}{\partial x_i}\right) \\
&\quad - \epsilon_{mij}\overline{\rho}\frac{\partial \Omega_i}{\partial x_j}\left[\frac{\partial}{\partial x_l}(\overline{u_m'' u_l''}) - \frac{\partial k}{\partial x_m}\right] \\
&\quad + (\alpha_3 b_{ij} + \frac{1}{3}\delta_{ij})\overline{\rho}\zeta\tilde{s}_{ij} - \frac{\beta_4 \tau_{ij}\Omega_i\Omega_j}{k\Omega} - \frac{\beta_5}{R_k + \delta}\overline{\rho}\zeta^{3/2} \\
&\quad - \frac{2\beta_6 \tau_{ij}\nu_t}{k\nu}\Omega\Omega_i\Omega_j + \frac{\beta_7\overline{\rho}\zeta}{\Omega^2}\Omega_i\Omega_j\tilde{s}_{ij} \\
&\quad + 2\beta_8\epsilon_{ilm}\left(\frac{\tau_{ij}}{k}\right)\frac{\partial k}{\partial x_l}\frac{\partial \zeta}{\partial x_m}\frac{\Omega_j}{\overline{s}^2 + \Omega^2/2} \\
&\quad + \max[P_\zeta, 0] - 2\overline{\rho}\zeta\tilde{s}_{ij} - C_{\zeta_1}\frac{\mu_t\zeta\Omega}{\tau_\rho k} \qquad (3.2)
\end{aligned}$$

All model constants in above equations are documented in [46].

In this model, the kinematic eddy viscosity is given by:

$$\nu_{t,RANS} = C_\mu\frac{k^2}{\nu\zeta} \qquad (3.3)$$

where $C_\mu = 0.09$.

For the LES component, the one-equation subgrid scale (SGS) model is given by

$$\frac{\partial \overline{\rho} k}{\partial t} + \frac{\partial \overline{\rho} \tilde{u}_j k}{\partial x_j} = \tau_{ij}\frac{\partial \tilde{u}_i}{\partial x_j} - C_d\frac{\bar{\rho}k^{3/2}}{\Delta} + \text{Diffusion} \qquad (3.4)$$

where τ_{ij} is the SGS stress tensor, Δ is the grid size, and C_d is a model constant. Here, we assume that the diffusion term is the same as that in Equation(3.1). Two versions of grid size are used in this work. The cell-volume based grid size is defined as,

$$\Delta_v = V^{1/3} \qquad (3.5)$$

where V is the volume of grid cell. The other choice of Δ is given by

$$\Delta_m = \max\left(\Delta_x, \Delta_y, \Delta_z\right) \tag{3.6}$$

where Δ_x, Δ_y, and Δ_z are the mesh spacings in three coordinate directions, respectively.

Under this one-equation model, the eddy-viscosity is calculated by

$$\nu_{t,LES} = C_s\sqrt{k}\Delta \tag{3.7}$$

where Δ is the same as that used in k equation. So it can be Δ_m or Δ_v.

For equilibrium conditions, where production equals dissipation, it follows from Equation(3.4) and Equation(3.7) that

$$\nu_{t,LES} \approx C_s\sqrt{\frac{C_s}{C_d}}\Delta^2\tilde{S} \tag{3.8}$$

which is equivalent to the Smagorinsky model[15].

To get an LES/RANS hybrid scheme, the one-equation SGS model, is blended with the k-equation of k–ζ model by a blending function Γ. The resulting k equation is given by:

$$\begin{aligned}\frac{\partial\overline{\rho}k}{\partial t} + \frac{\partial\overline{\rho}\tilde{u}_j k}{\partial x_j} &= \frac{\partial}{\partial x_j}\left[\left(\frac{\mu}{3} + \frac{\mu_t}{\sigma_k}\right)\frac{\partial k}{\partial x_j}\right] \\ &\quad +\tau_{ij}\frac{\partial\tilde{u}_i}{\partial x_j} \\ &\quad -(1-\Gamma)\left(\frac{1}{C_k}\frac{\mu_t}{\overline{\rho}^2}\frac{\partial\overline{\rho}}{\partial x_i}\frac{\partial\overline{P}}{\partial x_i} + C_1\frac{\overline{\rho}k}{\tau_\rho} + \mu\zeta\right) - \Gamma C_d\overline{\rho}\frac{k^{3/2}}{\Delta}\end{aligned} \tag{3.9}$$

ζ equation remains unchanged.

The hybrid eddy viscosity is then defined as:

$$\nu_t = (1-\Gamma)\nu_{t,RANS} + \Gamma\nu_{t,LES} \tag{3.10}$$

which is used to calculate the turbulent stresses τ_{ij}.

3.2 Blending Functions

One of the objectives in this research is to look for a blending function without explicit dependence on the wall distance. Recall that, in LES, *small* eddies need to be modeled. In other words, compared with the grid size, the size of the energy bearing eddies (integral length scale) determines the manner in which turbulence is modeled. If this size is much larger than grid size, then it can be mostly captured by using LES. Otherwise, RANS has to be used. Since the dissipation length scale l_ϵ:

$$l_\epsilon = \frac{k^{3/2}}{\nu\zeta}, \tag{3.11}$$

is of the order of the integral length scale[3], it can be used to construct the blending function. With different choices of grid size, we have the following two blending functions, called Γ_1 and Γ_2:

$$\Gamma_1 = \tanh\left(l_\epsilon/\alpha_1\Delta_m\right)^4 \tag{3.12}$$

and

$$\Gamma_2 = \tanh\left(l_\epsilon/\alpha_1\Delta_v\right)^2 \tag{3.13}$$

Here, α_1 is a model constant. Note that, from Equation(3.3), $\nu_{t,RANS}$ can be expressed as

$$\nu_{t,RANS} = C_\mu l_\epsilon\sqrt{k} \tag{3.14}$$

So Equation(3.3) and (3.7) yield that

$$\frac{l_\epsilon}{\alpha_1\Delta} \propto \frac{\nu_{t,RANS}}{\nu_{t,LES}} \tag{3.15}$$

When Γ_1 is used, $\Delta = \Delta_m$ is used in Equations(3.7) and (3.9). When Γ_2 is used, $\Delta = \Delta_v$ in those two equations.

To prevent Γ from decreasing in the freestream region as a result of small value of k, Γ must be a non-decreasing function as the distance from the wall increases. One way to implement this is to set:

$$\Gamma[j] = max(\Gamma[j], \Gamma[j-1]) \tag{3.16}$$

where j is the index of grid cell in the the direction normal to the wall. This mimics blending functions used in [31][32] that have explicit dependence on wall distance.

To choose a proper constant α_1, we need to analyze the length scale in the inner layer and outer layer of turbulent boundary-layer.

From the *law of the wall*, we have:

$$u = \frac{u_\tau}{\kappa} \ln\left(\frac{y u_\tau}{\nu_w}\right) + C$$

in log law region, where the friction velocity $u_\tau \equiv \sqrt{\tau_w/\rho_w}$, κ is von Karman's constant, and $C \approx 5.5$.

By differentiating above equation w.r.t. y, we have:

$$\frac{du}{dy} = \frac{u_\tau}{\kappa y}$$

Since, in this region, the turbulent stress $\tau \approx const$, and $k \approx const$, then $\nu_t \sim \kappa y$. But in log law region, Equation(3.7) has different behavior, because length scale Δ can be constant in a structured grid. Therefore, Equation(3.7) should be used in the outer region of a boundary layer, where the turbulence length scale $\sim \delta$, which is function of x.

Above blending functions, Γ_1 and Γ_2, depend on grid size. An alternative to the grid-dependent blending functions is to use von Karman length scale, l_s:

$$l_s \equiv \frac{\tilde{S}}{|\nabla \tilde{S}|} \tag{3.17}$$

where

$$\tilde{S} = \sqrt{\tilde{S}_{ij}\tilde{S}_{ij}} \tag{3.18}$$

l_s is a measure of the real size of turbulent eddies. In log-law layer, $l_s \propto y$. Therefore, l_s can be considered as an indication of the distance away from the wall. Based on this, another blending function, Γ_3, is defined as

$$\Gamma_3 = \tanh(\frac{l_s}{\alpha_1 \lambda})^2 \tag{3.19}$$

where λ is Taylor's microscale

$$\lambda = \sqrt{k/\zeta} \tag{3.20}$$

which lies in the inertial subrange – the range between the energy containing eddies and the viscous range. Thus, Γ_3 has no explicit dependence on the grid. In this research, when Γ_3 is used, $\Delta = \Delta_v$ is used in Equations(3.7) and (3.9). Equation(3.16) is also applied to this blending function.

Chapter 4

Turbulent Inflow Boundary Conditions

As described in foregoing chapters, the LES and therefore the LES/RANS hybrid scheme are time-dependent computations. This requires the inflow boundary condition to be unsteady.

In many baseline experiments for testing capability of high-speed turbulence modeling, inflow boundary layer is developed over a flat plate ahead of various experimental models. So, in this chapter, the method to provide turbulent inflow boundary conditions for the flow over a flat plate suited for hybrid LES/RANS calculation is presented.

4.1 Rescaling-Reintroducing Procedure

The current inflow turbulence generation method can be considered as a variant of rescaling-reintroducing method developed by Urbin *et al.*[40]. The procedure in [40], which is illustrated in Figure 4.1, consists of the following steps:

1. Get *mean values* and *fluctuations* from a downstream station, the recycle-plane;

2. Based on similarity, rescale above values;

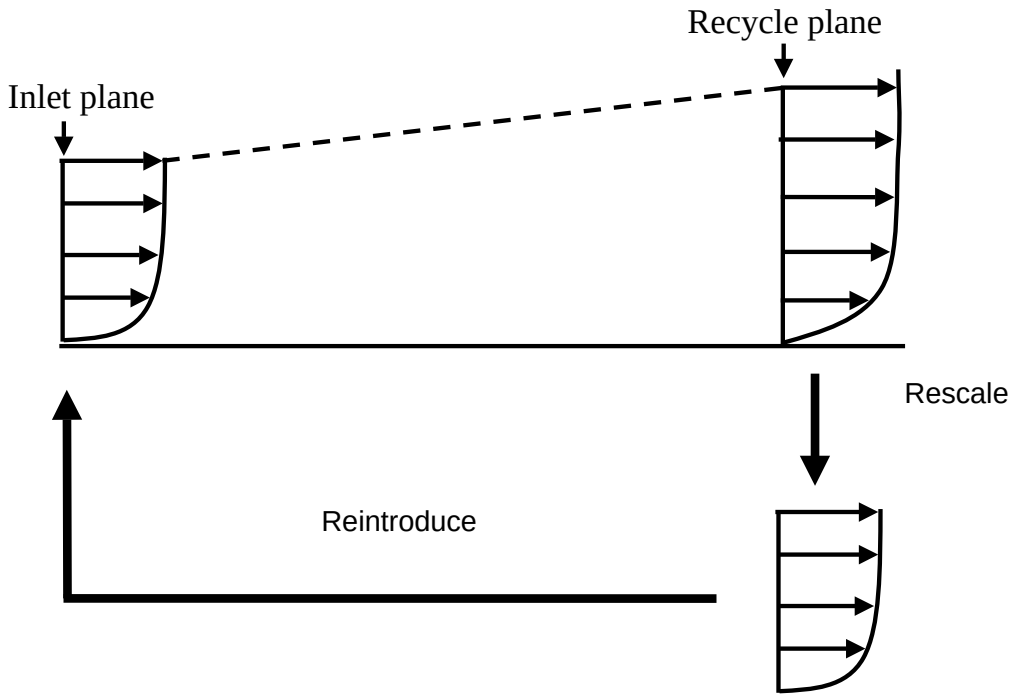

Figure 4.1: Rescaling-reintroducing procedure.

3. Introduce the rescaled value at the inlet station as an updated inflow boundary condition.

In [40], constant-coefficient SGS model and MILES model were employed. Thus, no additional equations for closure of governing equations are required. For current LES/RANS hybrid schemes, two extra model equations must be considered, and this will necessitate a modification of the procedure of [40].

Moreover, the need to match mean inflow conditions of experiments, such as momentum thickness, skin friction, *etc*., requires the inflow mean velocity and temperature profiles remain fixed. So the modified rescaling-reintroducing method can be described as:

1. Fix the inflow mean profiles of velocity and static temperature. Mean static pressure at inflow boundary is set equal to p_∞, the freestream static pressure, since we are dealing with the flow over flat plate. Then, mean density profile is determined from the equation of state.

2. Fluctuations of velocity and static temperature at recycle station is rescaled and superimposed onto the inflow mean profiles.

3. Mean values and fluctuations of k and ζ can be rescaled and reintroduced.

The general rescaling-reintroducing procedure is described as follows using the velocity for example.

Let $u(x, y, z, t)$ denote instantaneous velocity in x direction. It can be decomposed into two components:

$$u(x, y, z, t) = U(x, y) + u''(x, y, z, t) \tag{4.1}$$

$$U(x, y) = \frac{1}{t_f - t_i} \int_{t_i}^{t_f} \langle u \rangle dt \tag{4.2}$$

where U is the mean value, and u'' the instantaneous fluctuation. $\langle \cdot \rangle$ stands for the average over z-direction.

The multilayer scaling of a compressible boundary-layer makes use of an effective velocity developed by van Driest. The effective velocity is related to U by the relation[51]

$$U_{eff} = \frac{U_\infty}{A_1} \left[\sin^{-1} \left(\frac{2A_1^2 (U/U_\infty) - A_2}{\sqrt{A_2^2 + 4A_1^2}} \right) + \sin^{-1} \left(\frac{A_2}{\sqrt{A_2^2 + 4A_1^2}} \right) \right] \tag{4.3}$$

with

$$A_1 = \sqrt{\frac{(\gamma-1)}{2} r M_\infty^2 \left(\frac{T_\infty}{T_w}\right)}, \qquad A_2 = \frac{1 + \frac{(\gamma-1)}{2} r M_\infty^2}{T_w/T_e} - 1$$

where T_∞ and T_w are free stream and wall static temperature, respectively, M_∞ is the free stream Mach number, $r \approx Pr^{1/3}$ is the recovery factor, and $Pr = 0.7$ is the laminar Prandtl number.

By using the effective velocity, two similarity laws of compressible boundary-layer are:

$$U_{eff}^{inn} = u_\tau f_1(y^+), \qquad \text{law of the wall} \tag{4.4}$$

$$U_{eff}^{\infty} - U_{eff}^{out} = u_\tau f_2(\eta), \qquad \text{defect law} \tag{4.5}$$

where $\eta = y/\delta$ is nondimensional wall distance for outer layer, $y^+ = y u_\tau/\nu_w$ is nondimensional wall distance for inner layer, U_{eff}^{∞} is the effective velocity of U_∞, the freestream velocity. "inn" and "out" stand for inner and outer region of boundary layer, respectively.

According to the two similarity laws, we can have the following two transformations for the fluctuations of velocity:

$$u_{inlet}^{\prime\prime inn} = \beta u_{recy}^{\prime\prime inn}(y_{inlet}^+, z, t) \tag{4.6}$$

$$u_{inlet}^{\prime\prime out} = \beta u_{recy}^{\prime\prime out}(\eta_{inlet}, z, t) \tag{4.7}$$

where $\beta = u_{\tau,inlet}/u_{\tau,recy}$, "$inlet$" and "$recy$" denote the inlet station and the recycle station, respectively.

The wall-normal velocity fluctuation v'' and the spanwise velocity fluctuation w'' are scaled similarly.

Then, the complete velocity fluctuations are the weighted average values of inner and outer fluctuation profiles, which are given by[34][40]:

$$u''_{inlet} = u''^{inn}_{inlet}[1 - W(\eta_{inlet})] + u''^{out}_{inlet} W(\eta_{inlet}) \tag{4.8}$$

where, the weight function is defined as

$$W(\eta) = \frac{1}{2}\left(1 + \left\{\tanh\left[\frac{4(\eta - B)}{(1-2B)\eta + B}\right]\right\}\right) \tag{4.9}$$

where $B = 0.2$. Thus the weight function have a smooth switch[34][40] at $y/\delta = 0.2$.

With the fixed inlet mean velocity profiles, the complete inlet velocity is given by:

$$u_{inlet} = U_{inlet} + u''_{inlet} \tag{4.10}$$

Other velocity components can be processed similarly.

β and $\delta_{inlet}/\delta_{recy}$, as suggested in [40], can be derived from power law[52], $U/U_\infty = (y/\delta)^{\frac{1}{n}}$. For $n = 9$, we have

$$\frac{\delta_{recy}}{\delta_{inlet}} = \left[1 + 0.27\frac{L}{\delta_{inlet}} Re_{\delta_{inlet}}^{-\frac{1}{5}}\right]^{\frac{5}{6}} \tag{4.11}$$

$$\frac{u_{\tau,recy}}{u_{\tau,inlet}} = \left(\frac{\delta_{recy}}{\delta_{inlet}}\right)^{\frac{1}{10}} \tag{4.12}$$

where L is the distance between inlet station and recycle station, Re_δ is the Reynolds number based on boundary layer thickness.

4.2 Scaling of k, ζ and T, ρ

To give complete inflow boundary condition in the LES/RANS hybrid scheme, we need to specify, in addition to velocity, density, temperature, k and ζ at the inlet station. Based

on Morkovin's assumption[53], the pressure fluctuations at modest high speed flow ($M < 5.0$) are negligible. Hence, pressure at inlet station of a flat plate can be set equal to the freestream pressure p_∞. Then from the equation of state, density only depends on the temperature. In this case, the scaling of k, ζ and $\tilde{T}$ plus the scaling of velocity presented in last section can give the desired set of inflow boundary conditions.

The LES formulation does not include equations for k–ζ model, but these quantities can be calculated as part of the solution, if desired. Because of this, both mean value and fluctuations of k and ζ are rescaled and reintroduced into the inlet plane. The proper scaling of these quantities can be derived from the governing equations in the log law layer[54].

In the log law layer, the energy equation reduces, for an insulated wall, to (c.f. Equation(5.77) in [3])

$$\frac{C_p\tilde{T}}{Pr_t} + \frac{\tilde{u}^2}{2} + \frac{k}{\sigma_k} = \frac{C_p}{Pr_t}\tilde{T}_w \tag{4.13}$$

or

$$\frac{C_p}{Pr_t}\left(\tilde{T} - \tilde{T}_w\right) + \frac{\tilde{u}^2}{2} + \frac{k}{\sigma_k} = 0 \tag{4.14}$$

Thus, since $\tilde{u}$ scales with u_τ, k must scale with u_τ^2, and $(\tilde{T} - \tilde{T}_w)$ must scale with u_τ^2. If q_w is not zero, then the energy equation can be recast in the form given by Equation (5.83) in [3], i.e.

$$\frac{d}{d\tilde{u}}\left(\frac{C_p\tilde{T}}{Pr_t} + \frac{\tilde{u}^2}{2} + \frac{k}{\sigma_k}\right) = -\frac{q_w}{\tilde{\rho}_w u_\tau^2} \tag{4.15}$$

Since

$$\begin{aligned} q_w &= -\frac{\mu C_p}{Pr}\left(\frac{\partial \tilde{T}}{\partial y}\right)_{y=0} \\ &= -\frac{\mu C_p}{Pr}\left(\frac{d\tilde{T}}{d\tilde{u}}\right)_{\tilde{u}=0}\left(\frac{d\tilde{u}}{dy}\right)_{y=0} \\ &= -\frac{C_p}{Pr}\left(\frac{d\tilde{T}}{d\tilde{u}}\right)_{\tilde{u}=0}\tau_w \end{aligned} \tag{4.16}$$

It can be seen, from Equation(4.16), that q_w scales like u_τ^3.

Integration of Equation(4.15) is given by Equation(5.86) in [3]. It is seen from the equation and the equation of state that, for a flat plate,

$$\frac{\tilde{T}}{\tilde{T}_w} = \frac{\bar{\rho}_w}{\bar{\rho}} = 1 - (\gamma - 1) Pr_t M_\tau^2 \left[\frac{1}{2}\left(\frac{\tilde{u}}{u_\tau}\right)^2 + \frac{q_w}{\bar{\rho}_w u_\tau^3}\left(\frac{\tilde{u}}{u_\tau}\right) + \left(\frac{k}{\sigma_k u_\tau^2}\right)\right] \tag{4.17}$$

where

$$M_\tau = \frac{u_\tau}{a_w} \tag{4.18}$$

Thus, in the inner region(log law region) where $y^+_{inlet} = y^+_{recy}$, the scaling rules are

$$\left(\frac{\tilde{T}}{\tilde{T}_w} - 1\right)^{inn}_{inlet} = \beta^2 \left(\frac{\tilde{T}}{\tilde{T}_w} - 1\right)^{inn}_{recy} \tag{4.19}$$

$$\left(\frac{T''}{\tilde{T}_w}\right)^{inn}_{inlet} = \beta^2 \left(\frac{T''}{\tilde{T}_w}\right)^{inn}_{recy} \tag{4.20}$$

$$k^{inn}_{inlet} = \beta^2 k^{inn}_{recy} \tag{4.21}$$

$$\left(\frac{\nu \nu_w \zeta}{u_\tau^4}\right)^{inn}_{inlet} = \left(\frac{\nu \nu_w \zeta}{u_\tau^4}\right)^{inn}_{recy} \tag{4.22}$$

Note that for the scaling of temperature, only the scaling of fluctuations is used in the rescaling-reintroducing procedure, since the inflow mean profile of temperature is fixed at the inlet.

In the outer region of boundary layer where $\eta_{inlet} = \eta_{recy}$, we assume

$$\left(\frac{T''}{\tilde{T}_w}\right)^{out}_{inlet} = \beta^2 \left(\frac{T''}{\tilde{T}_w}\right)^{out}_{recy} \tag{4.23}$$

In this region, based on Equation(4.162) of [3], k and ζ scale like

$$k^{out}_{inlet} = \beta^2 k^{out}_{recy} \tag{4.24}$$

$$\left(\frac{\delta\nu\zeta}{u_\tau^3}\right)^{out}_{inlet} = \left(\frac{\delta\nu\zeta}{u_\tau^3}\right)^{out}_{recy} \tag{4.25}$$

Chapter 5

Implementation

The LES/RANS hybrid schemes have been evaluated by comparing the results with two experimental shock wave / boundary layer interaction databases . The first one corresponds to the compression-expansion ramp experiment of Zheltovodov *et al.*[55; 56], while the other, also available in [55], involves a compression ramp experiment by Settles *et al.* Both cases have observable separation zones around the compression corner.

This chapter will introduce both configurations, inflow conditions, and grids. Also in this chapter, the special computation procedure for simulating the flows with LES/RANS hybrid schemes will be presented, which will prevent the separation zone from growing to the extent that may affect inflow conditions. The numerical schemes for solving the system of equations will be presented in Appendix B.

5.1 Zheltovodov 25 deg Compression-Expansion Ramp

The computational domain of this two dimensional configuration is shown in Figure 5.1. It consists of a $8\ cm$ long flat plate and a 25 deg compression ramp, which is followed by wedge-expansion corner. The hight of the ramp is $1.5\ cm$.

Two meshes are employed in this investigation. A coarse grid which consists of $361 \times$

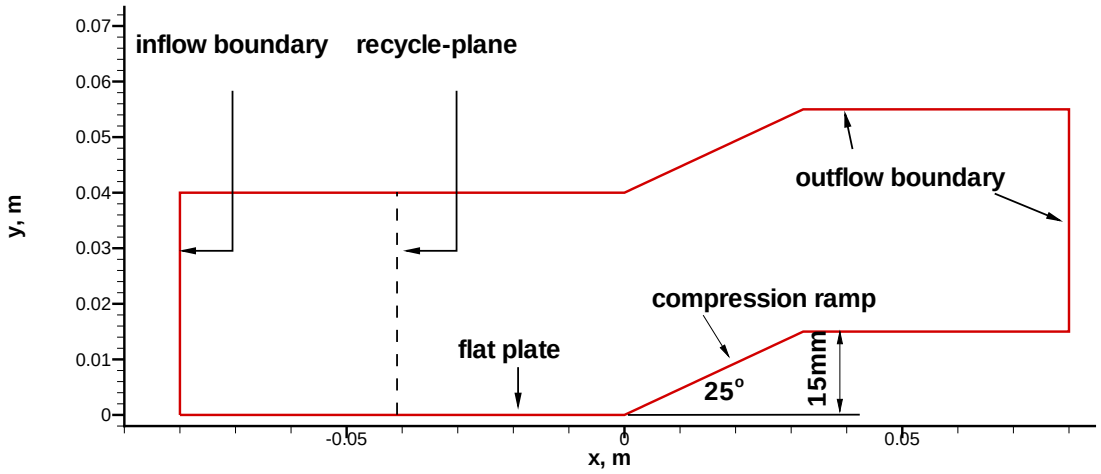

Figure 5.1: Zheltovodov 25 deg Ramp.

109×65 nodes, and a fine grid which consists of $481 \times 145 \times 65$ nodes. In both cases, the physical size of the grid in the z-direction is equal to 2.9δ, where δ is boundary layer thickness at inflow. Both grids are uniformly spaced in the x- and z-direction, and clustered heavily towards the wall in the y-direction. The $y^+ \leq 1$ for the center of the first cell is maintained at the inflow boundary. The whole domain is decomposed into $12 \times 4 \times 2$ equal-size blocks and solved on 96 processors using IBM-SP3 supercomputer.

The inflow conditions at $x = -3.3\ cm$ are presented in Table 5.1. A boundary layer code and a 2D RANS code were used to generate the desired boundary layer momentum thickness, θ, at this position by calculating a supersonic flow over a flat plate. Therefore, the resulting boundary layer thickness, δ, may be different from the experiment data. The δ from the computation was used to decide the spanwise size of the grid.

The inflow boundary condition for the computation domain is generated by recycling

Table 5.1: 25 Ramp Inflow Conditions @ x=-3.3 cm

M_∞	2.88
$P_\infty(Pa)$	11956
$T_\infty(K)$	114.8
$\rho_\infty(kg/m^3)$	0.36
$Re/meter$	3.24×10^7
$\theta(mm)$	0.3
$\delta(mm)$	4.1

and rescaling the information from the y-z plane at $x = -4.1\ cm$. Adiabatic and no-slip boundary conditions are applied to the wall surface. Since the flow is statistically two dimensional, periodic boundary condition is applied in the z-direction.

In this case, a time step of 6×10^{-8} seconds is used for the simulation. Therefore, 10k iterations is equivalent to 6×10^{-4} seconds physical time, which corresponds to 2.3 characteristic times. One characteristic time is defined as the time it takes for a particle to traverse the domain with free stream velocity.

5.2 Settles 20 deg Compression Ramp

The configuration of this ramp is shown in Figure 5.2. A $20\ cm$ flat plate is connected to a 20 deg ramp. The grid for this domain consists of $449 \times 129 \times 65$ nodes. Spanwise size is also set as 2.9δ. Similar to previous grids, equal mesh spacing is used in the x- and z-direction, and the mesh spacing in the y-direction is refined near the wall, with $y^+ \leq 1$ for the first cell center at the inflow boundary. It has been decomposed into $14 \times 3 \times 2$ blocks. The experimental data at $x = -3.81\ cm$ is listed in Table 5.2. For this configuration, recycle-plane is located at $x = -10.3\ cm$. Similarly, adiabatic and no-slip boundary

conditions are employed at the wall. Extrapolation condition is used at the outflow boundary, and periodic boundary condition in the z-direction. A 2D RANS code was used to match the experimental boundary layer thickness, δ.

In this case, the length of time step is 1.2×10^{-7} seconds. Hence, 10k iterations can simulate about 1.93 characteristic times.

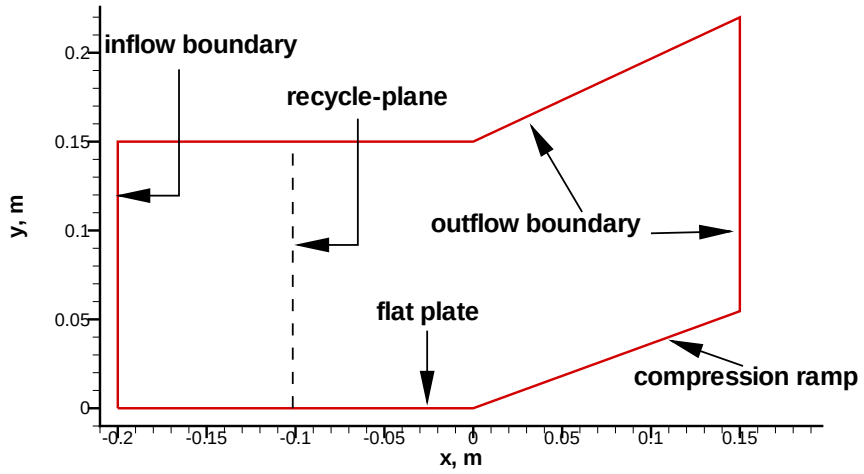

Figure 5.2: Settles 20 deg Ramp.

Table 5.2: 20 Ramp Inflow Conditions @ x=-3.81 cm

M_∞	2.79
$P_\infty(Pa)$	26001
$T_\infty(K)$	100.8
$\rho_\infty(kg/m^3)$	0.77
$Re/meter$	7.2×10^7
$\delta(cm)$	2.7

5.3 Computation Procedure

In Fan's thesis [33], the LES/RANS computation was conducted from a 2D RANS solution. In general, this approach may not succeed when a separation bubble is embedded in the initial flow. This is because the energy of the incoming fluctuations may not be sufficient at initial stage to prevent the growth of the separation bubble beyond the recycle-plane. To prevent the problem, a different approach is employed. The steps employed are as follows:

1. Match experimental boundary layer data. In this step, a boundary layer code or a two dimensional RANS code are used to calculate the flow over a flat plate. For example, for the 20 deg ramp case, once the 2D RANS code finds the location where the boundary layer thickness equals $2.7\ cm$, the boundary layer data at $20 - 3.81 = 16.19\ cm$ upstream of that station will be taken as the inflow condition for computational domain of the 2D ramp.

2. Use the inflow boundary data from step 1 and two dimensional RANS code to calculate the two dimensional steady RANS solutions. Note that step 1 and step 2 prepare the initial flow field for the applications of LES/RANS hybrid schemes, which start from step3.

3. Build up the turbulent fluctuations over flat plate. Only the grid on the flat plate part is involved. The grid size is half the ramp grid size. The flow field over the flat plate is initialized with the inflow boundary layer profile (obtained from step 1). Then random perturbations are imposed on the whole domain to generate initial fluctuations. This step is finished when large enough turbulence fluctuations are generated. For the 25 deg ramp case, the criteria of "large enough" is that the maximum *RMS* mass flow fluctuation reaches

$0.08\rho_\infty u_\infty$, while for the 20 deg ramp case, it is $0.04\rho_\infty u_\infty$. Figure 5.3 is an example of the resulting flow over the flat plate of 25 deg ramp case.

4. Start solving ramp problem. To initialize the flow field, the solutions from step 3 are combined with the steady RANS solution of the ramp. A snapshot of the combined initial flow field is presented in Figure 5.4. Note that the data in the last column of blocks in Figure 5.3, which include the grid and the flow properties, have been replaced with the RANS solution.

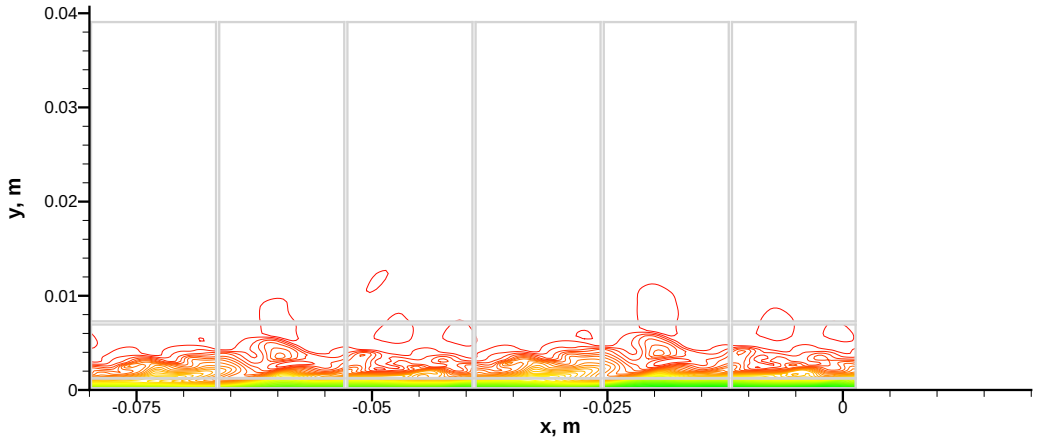

Figure 5.3: Turbulent fluctuations on flat plate: contour plot of u.

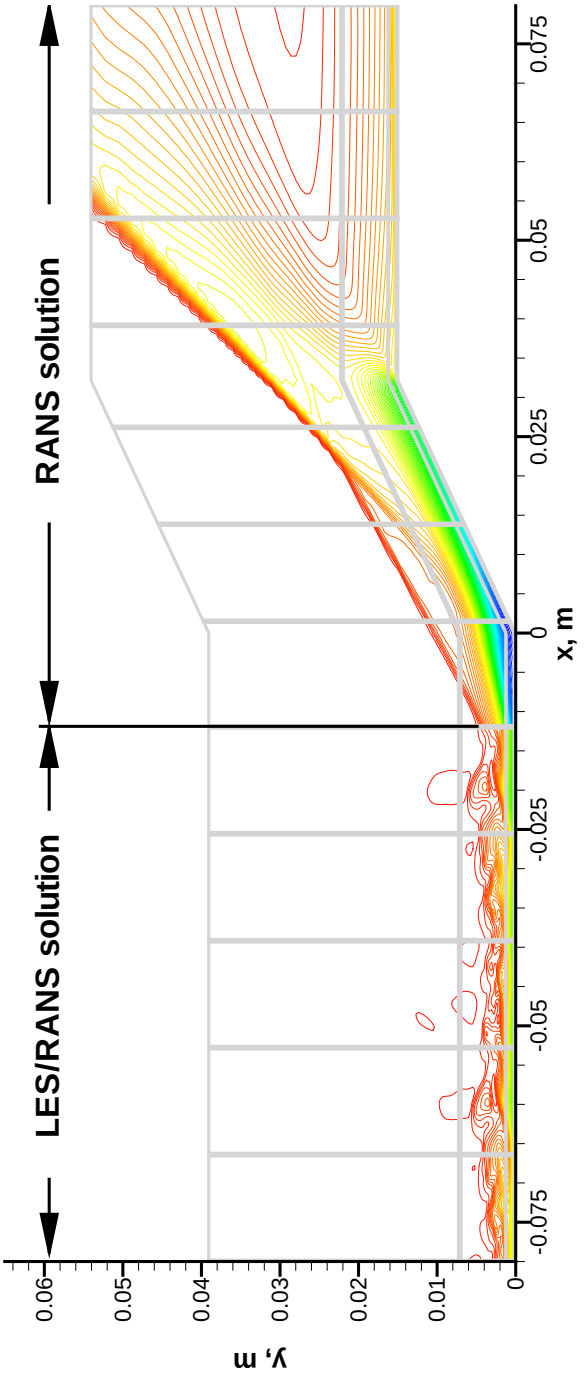

Figure 5.4: A combined initial solution: contour plot of u.

Chapter 6

Results and Analysis

This study is composed of two subtasks: the turbulent inflow boundary condition generation and the LES/RANS hybrid schemes. The comparison of different rescaling-reintroducing schemes will be presented in section 6.1. The rest of this chapter will present the results from different hybrid schemes on two shock wave/boundary layer interaction problems.

6.1 Inflow Turbulence Generation Scheme and Monotonic Blend Function

The inflow generation method has been tested for the flow over a flat plate.The dimension of the domain is $0.1m \times 0.092m \times 0.087m$. The grid size is $129 \times 129 \times 65$. This grid, with the exception of the extent of the flow in the z-direction, is almost the same as the one on the flat plate part of the 20 deg ramp. The entire domain is decomposed into $8 \times 4 \times 2$ blocks, when running on IBM-SP3 supercomputer. The recycle-plane is located at 6-cell upstream of the outflow boundary. The free stream conditions are the same as those for the 20 deg ramp. The inflow boundary thickness, $\delta = 3.0\ cm$.

To validate the LES/RANS rescaling-reintroducing scheme introduced in Chapter 4 and the monotonic blending function, the following four cases have been investigated.

Case 1 Both mean and fluctuations of all properties are rescaled and reintroduced to the inflow boundary. The monotonicity of Γ is not enforced in this case.

Case 2 Use the same rescaling-reintroducing scheme as case 1. But a monotonic Γ is used.

Case 3 Use the inflow turbulence generation method described in Chapter 4. The monotonicity of Γ is not enforced.

Case 4 Use the same rescaling-reintroducing scheme as case 3. And Γ is monotonic.

In these cases, the blending function Γ_1 is used. The model constant $\alpha_1 = 5$ is used so as to ensure that the transition from the RANS region to the LES region occurs above the log law layer. $C_s = 0.01$ and $C_d = 0.01$ are used for all cases of tests, and the ramp problems, these are the values used in [31; 32].

All results presented in this section are taken from the recycle-plane. Two versions of average value are presented in this section. For the *RMS* mass flow fluctuation, the average is based on time average, i.e. Equation(4.2). The *RMS* mass flow fluctuation is approximated by

$$\sqrt{\overline{\langle \rho u'' \rangle^2}} \approx \sqrt{\overline{\langle \rho u \rangle^2} - \overline{\langle \rho u \rangle}^2} \tag{6.1}$$

Overbar denotes the time average. $\langle \cdot \rangle$, again, means the average in spanwise direction.

Other average values are calculated using the following weighted average formula[34]:

$$U^{n+1} = \frac{\Delta t}{t_c} \langle u^{n+1} \rangle + \left(1 - \frac{\Delta t}{t_c}\right) U^n \tag{6.2}$$

where Δt is the computational time step, and t_c is the characteristic time scale of the averaging interval. $t_c \approx 5\delta/U_\infty$ is used. This formula can suppress starting transients quickly[34].

The history of boundary layer velocity profile of case 1 on the recycle-plane is shown in Figure 6.1, where averaged velocity profile does not reach statistical steadiness.

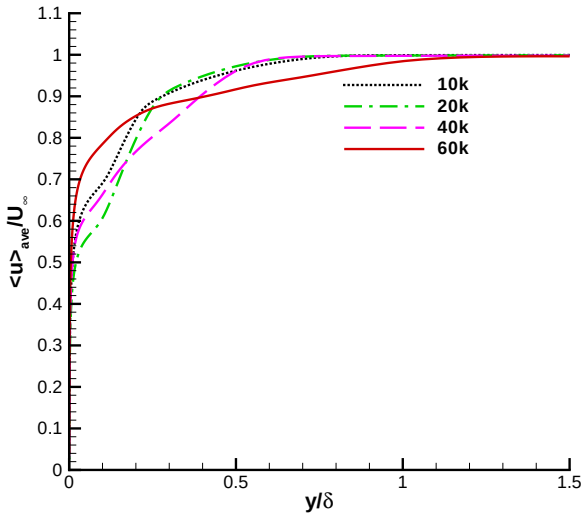

Figure 6.1: Mean streamwise velocity profiles, case 1.

In case 2, Γ is forced to be monotonic using Equation(3.16). The velocity profiles after each 10k iteration are presented in Figure 6.2. Similar to case 1, boundary profiles are not stabilized, which means a statistically steady turbulence flow is not available. Comparing case 1 with case 2, the incapability of generating desired mean inflow condition for the downstream computation is due mainly to the inappropriate rescaling-reintroducing method.

After fixing the inlet mean velocity and temperature profiles, we can see, from Figure 6.3, that there is little change in velocity profiles during the 50k iterations.

Figure 6.4 shows that the *RMS* mass flow fluctuation keeps increasing as the number

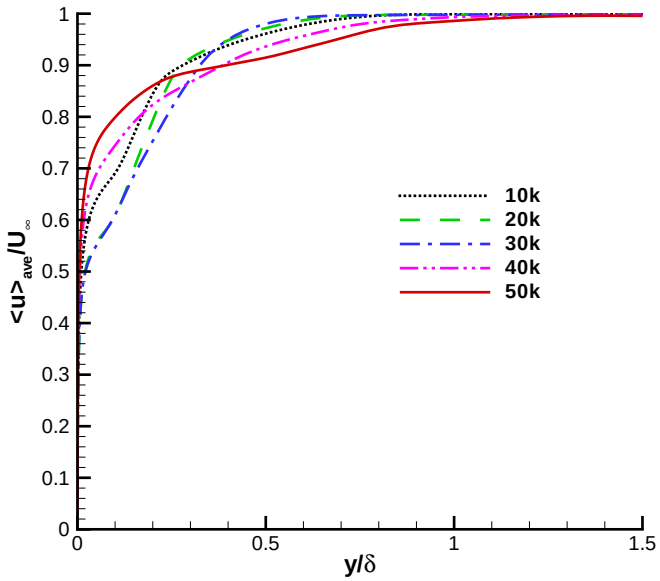

Figure 6.2: Mean streamwise velocity profiles, case 2.

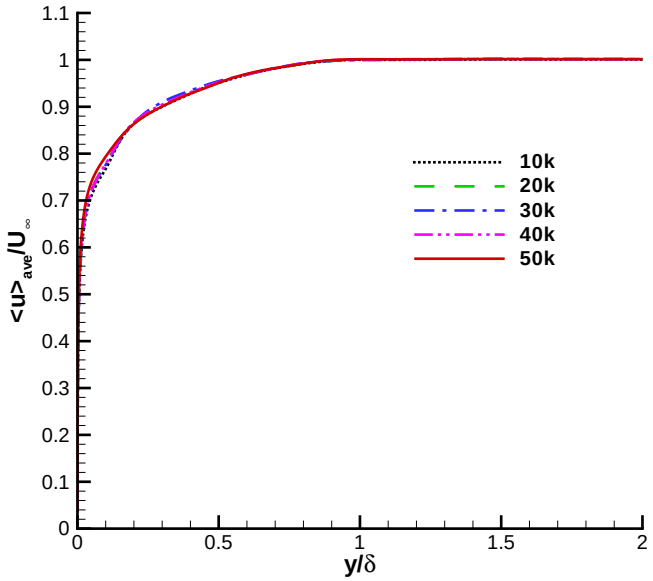

Figure 6.3: Mean streamwise velocity profiles, case 3.

of iterations increases. Moreover, the eddy viscosity (Figure 6.5) shows a similar behavior. The reason for this can be found in Figure 6.6, which shows the relation of Γ *vs* wall

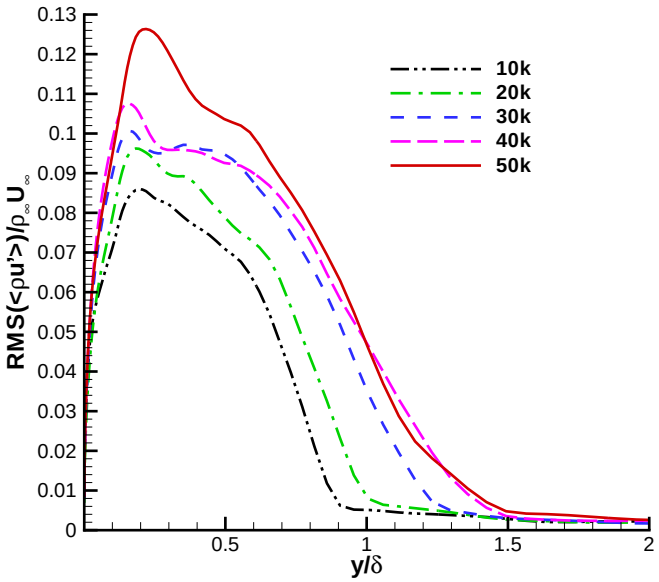

Figure 6.4: Profiles of *RMS* mass flow fluctuations, case 3.

distance. For $y/\delta > 1$, Γ decreases, which indicates a return to the RANS description. This is not consistent with the LES/RANS hybrid approach. Therefore, in order to prevent such a behavior, Γ should not be allowed to decrease in an increasing direction away from the wall.

In case 4, monotonicity is introduced by using Equation(3.16). Since the inflow mean profiles of velocity and temperature are fixed, the mean velocity profile on the recycle-plane is not affected by the new version of Γ, as is shown in Figure 6.7.

Figure 6.8 presents the *RMS* mass flow fluctuation profiles of this case. The maximum value of the quantity increases in the first 40k iterations. Then, it decreases. But the behavior beyond y/δ=1 is stabilized after 20k iteration.

Figure 6.9 shows the distribution of Γ. Compared to Figure 6.6, the profiles of Γ do not change as the number of iterations increases. Similar behavior for μ_t can be seen in

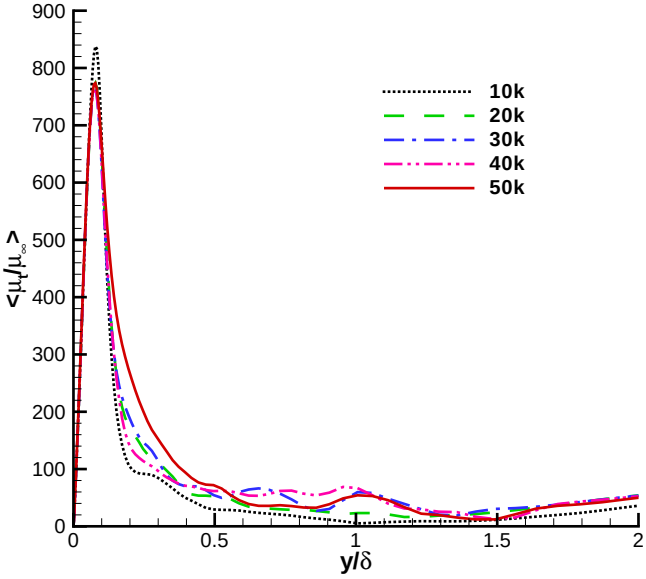

(a)

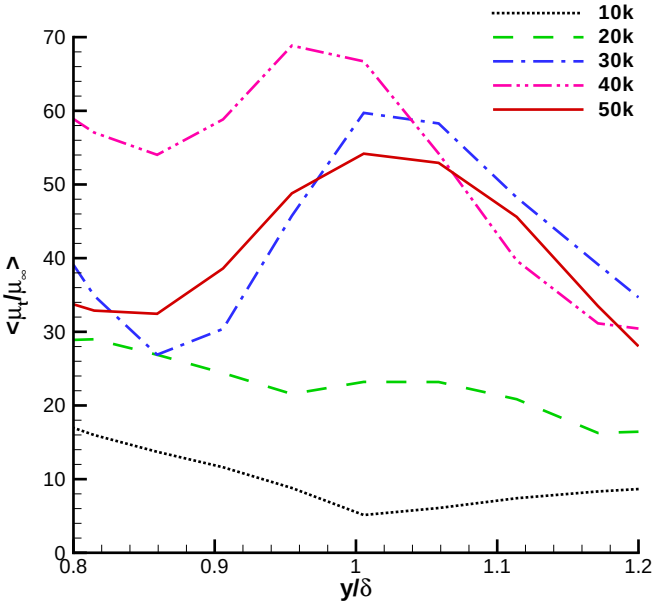

(b) at the edge of boundary layer

Figure 6.5: Profiles of mean eddy viscosity, case 3.

Figure 6.10. These indicate the statistical steadiness.

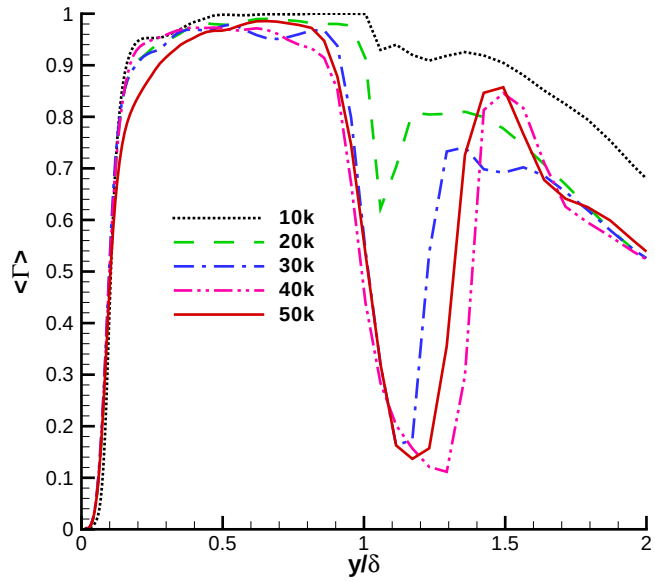

Figure 6.6: Profiles of blending function Γ, case 3.

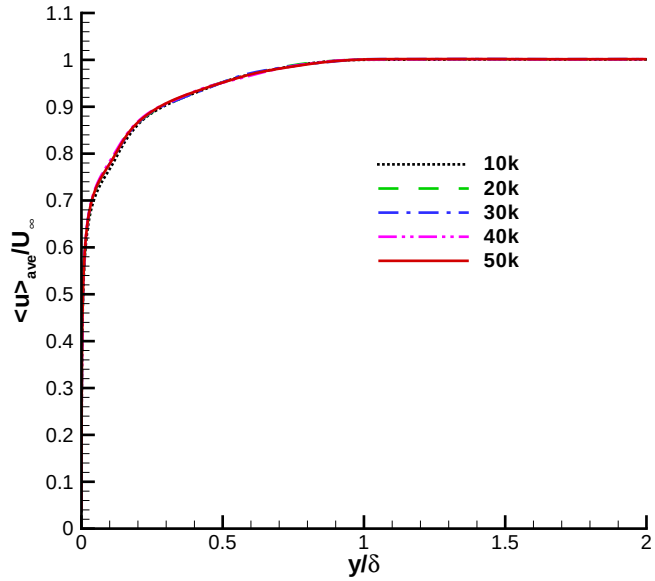

Figure 6.7: Mean streamwise velocity profile, case 4.

Figure 6.11 compares the mean streamwise velocity. The results after 40k and 50k iterations are in good agreement with the solution from the boundary layer code, except in

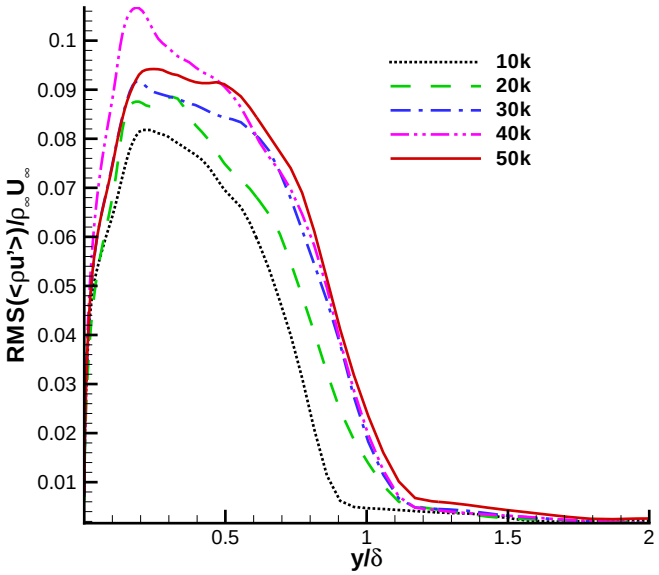

Figure 6.8: Profiles of *RMS* mass flow fluctuations, case 4.

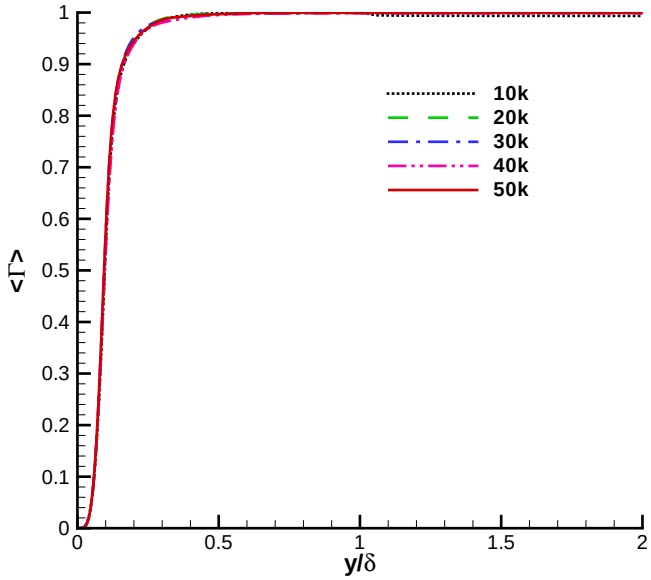

Figure 6.9: Profiles of blending function Γ, case 4.

the "grey region"[17], which lies between the RANS region ($\Gamma = 0$) and the LES region ($\Gamma = 1$). Similar to the results of Nikitin *et al.*[17], the slope and the intercept of log law

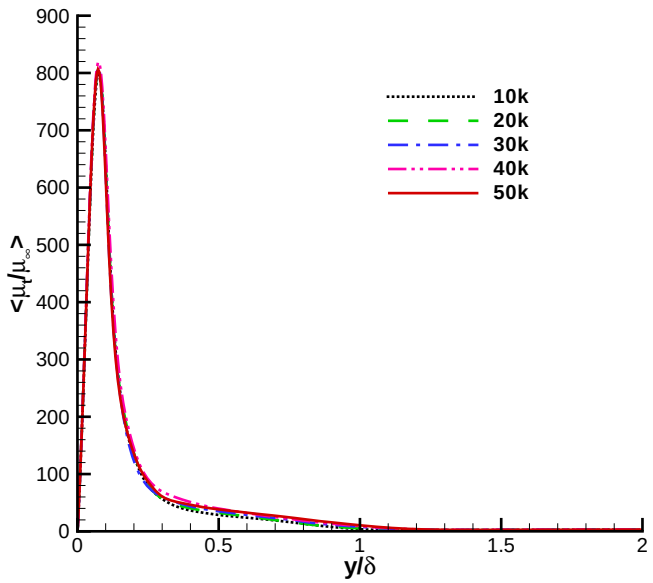

Figure 6.10: Profiles of mean eddy viscosity, case 4.

profile in the LES region is different from that in the RANS region. The good agreement with the solution of the boundary layer code in the near wall region can also be found in the k profile in Figure 6.12.

Figure 6.13 and Figure 6.14 are contour plots of instantaneous temperature on the x-y and y-z planes, respectively. The turbulence structure is apparent in both figures.

6.2 25 Ramp Flow

The instantaneous streamwise velocity distribution from a run of 40k iterations is shown in Figure 6.15. The large size of eddies in the incoming boundary layer is evident. Other features in this flow include the leading shock wave generated by the flow separation around the compression corner and an embedded shock wave due to the flow reattachment to the

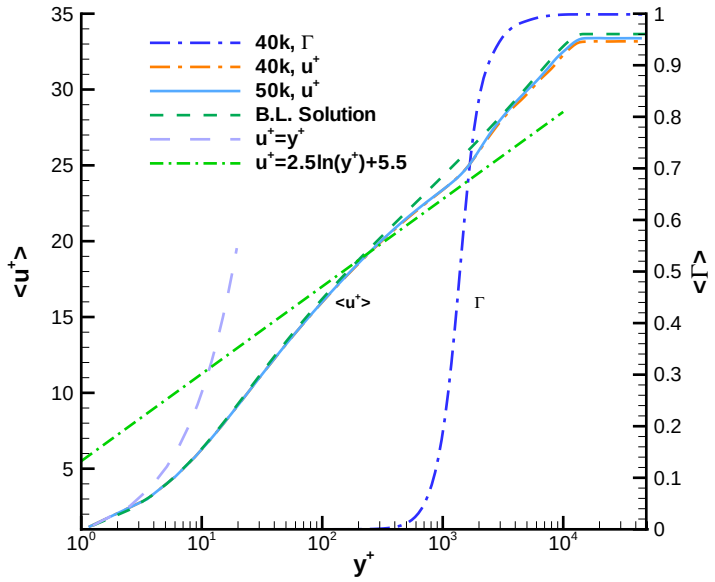

Figure 6.11: Profiles of mean streamwise velocity , case 4.

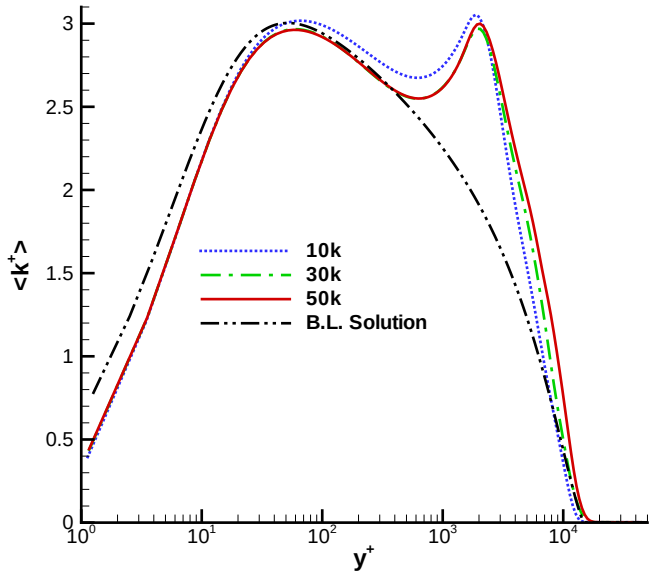

Figure 6.12: Profiles of mean k profile, case 4.

ramp surface.

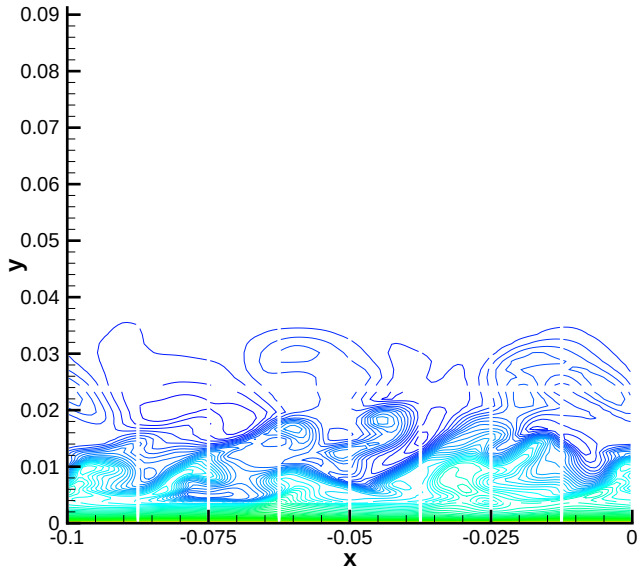

Figure 6.13: Instantaneous temperature in x-y plane, case 4.

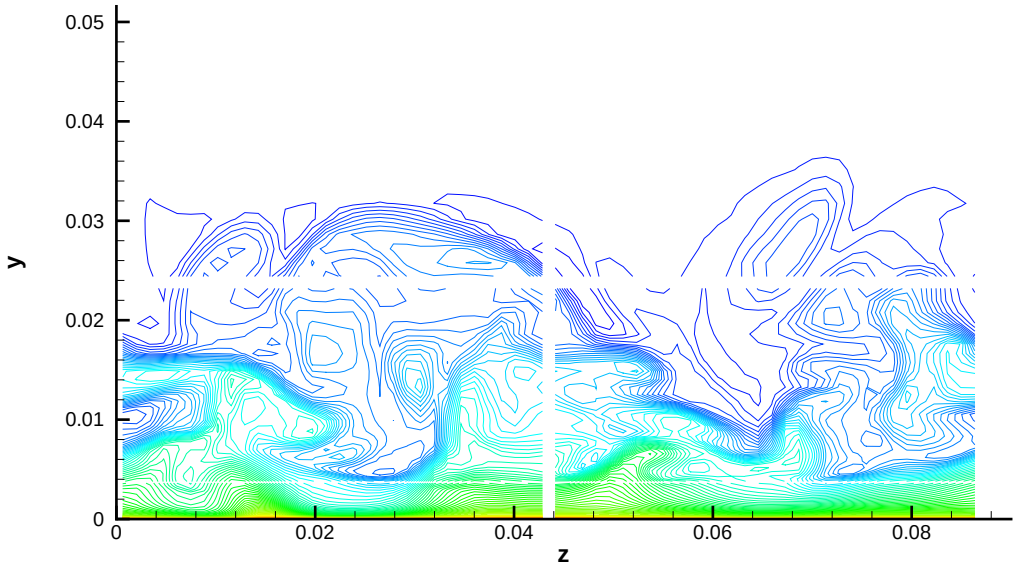

Figure 6.14: Instantaneous temperature in y-z plane, case 4.

The time-averaged data presented in this section are collected at the end of 40k iterations. Unless indicated otherwise, the average quantities are averaged over the last 10k

iterations. The x'-coordinates appearing in most of the figures are measured from an origin at the compression corner along the surface of the model, whether horizontal or at an angle[55].

6.2.1 Effects of Starting Procedure

All 25 deg ramp computations follow the procedure introduced in Section 5.3. The solution on the flat plate is prepared using Γ_1 with $\alpha_1 = 5.0$. The *RMS* mass fluctuations on the recycle-plane over every 10k iterations are shown in Figure 6.16. After 30k iterations, the *RMS* mass flow fluctuation can be considered as stabilized.

The skin friction(Figure 6.17) and the time-averaged wall pressure(Figure 6.18) indicate that the flow separation has little influence on the recycle-plane and the region upstream of it. Thus, the inflow turbulence is not disturbed by the separation bubble. Figure 6.19 and Figure 6.20 show the differences among the LES/RANS hybrid scheme, RANS and experimental data. When Γ_1 scheme is used, the size of the separation zone, indicated by negative skin friction, is much smaller than that predicted by the RANS. But the initial separation shock wave, indicated by the drop of C_f and the initial rise of wall pressure, is moved upstream in the LES/RANS solution. In the recovery region, the predicted skin friction is much larger than the RANS solution This phenomenon might be due to the small LES region above the ramp surface resulting from current blending function Γ_1.

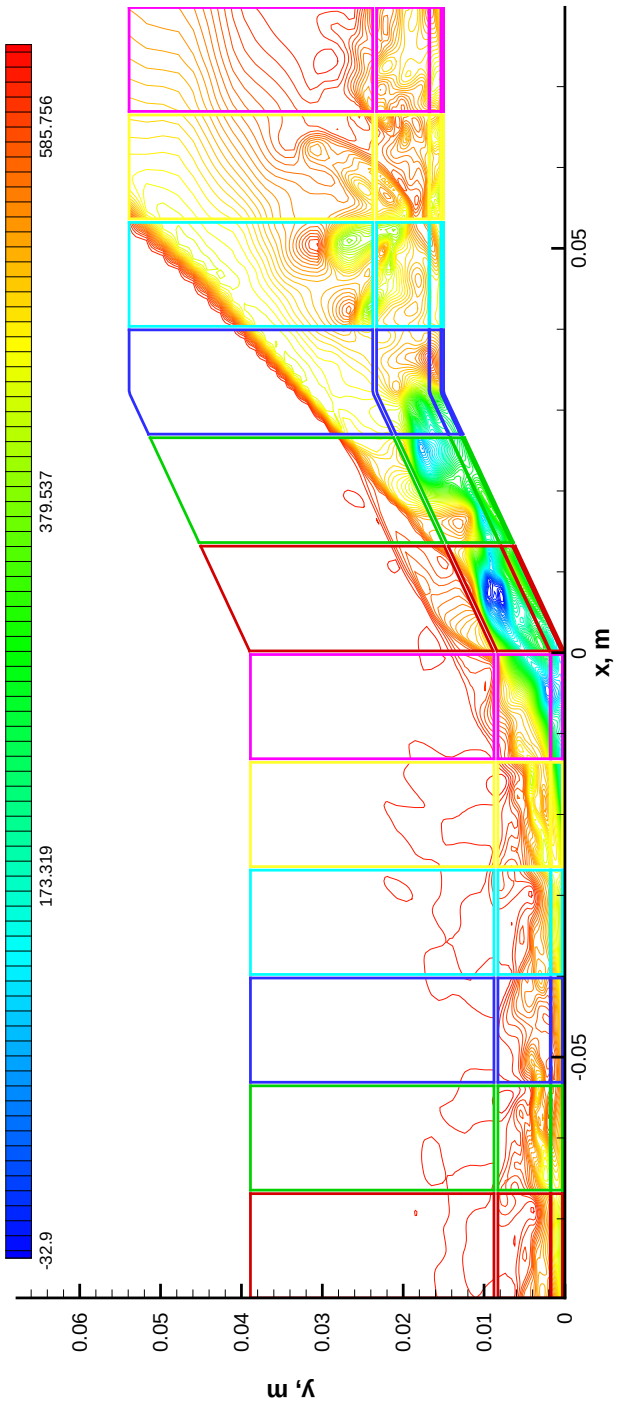

Figure 6.15: 25 Ramp: Instantaneous streamwise velocity(u) distribution.

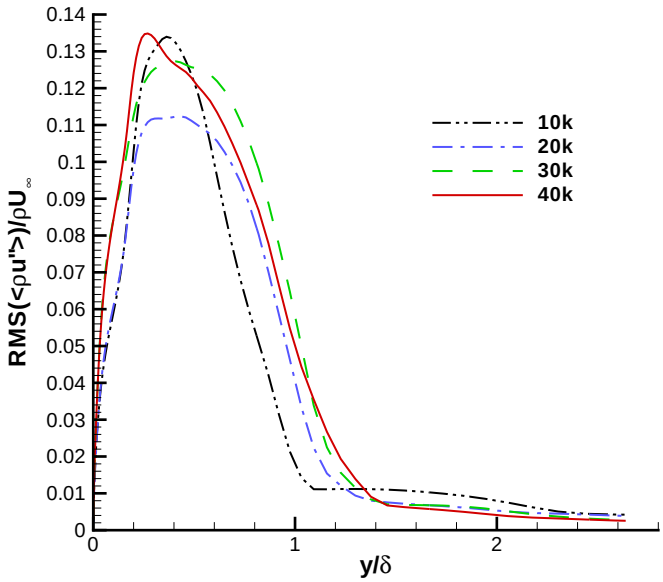

Figure 6.16: 25 Ramp: *RMS* mass flow fluctuation on recycle-plane, $\Gamma_1 = \tanh(\frac{l_\epsilon}{5\Delta_m})^4$

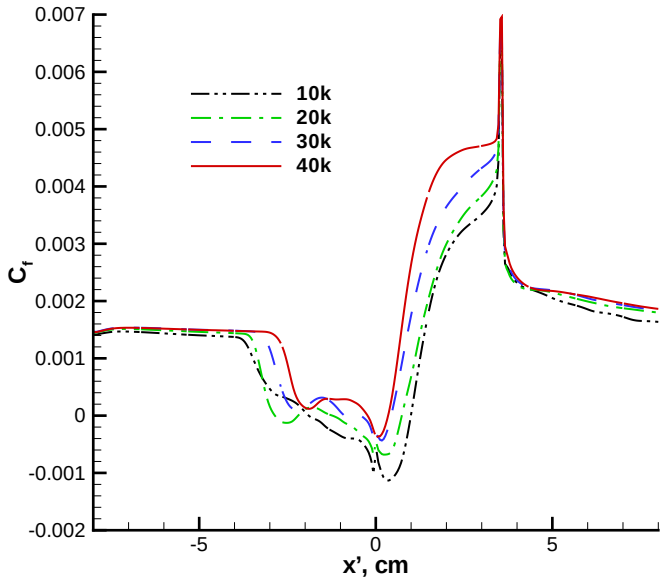

Figure 6.17: 25 Ramp: Skin friction distribution, $\Gamma_1 = \tanh(\frac{l_\epsilon}{5\Delta_m})^4$.

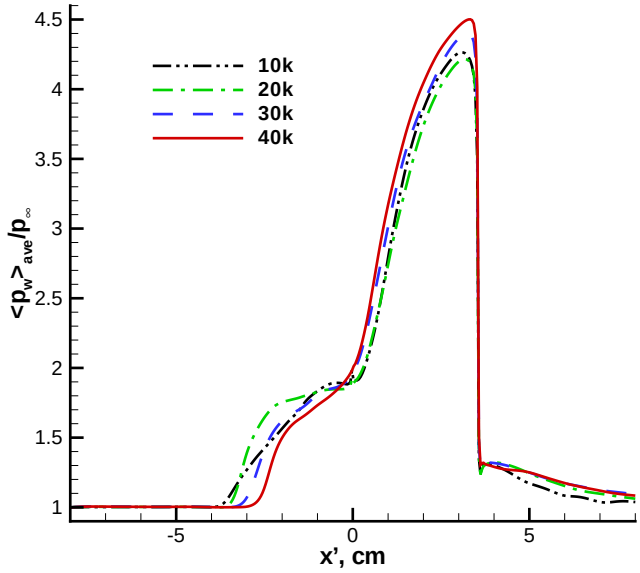

Figure 6.18: 25 Ramp: Wall pressure distribution, $\Gamma_1 = \tanh(\frac{l_\epsilon}{5\Delta_m})^4$.

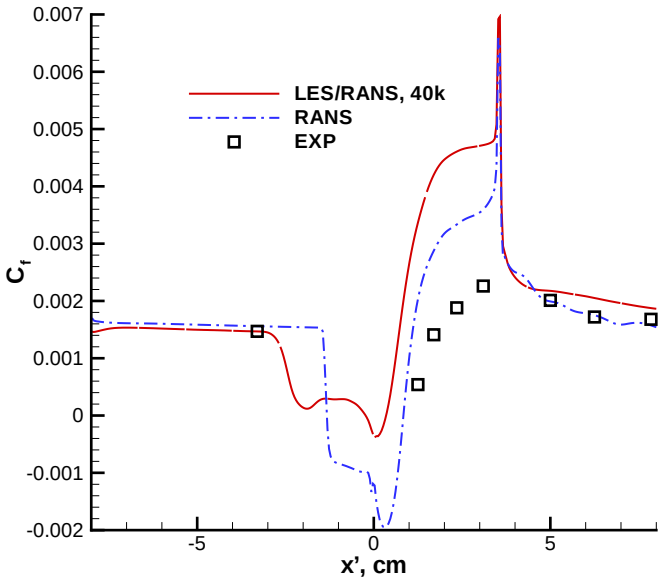

Figure 6.19: 25 Ramp: Comparison of skin friction distribution, $\Gamma_1 = \tanh(\frac{l_\epsilon}{5\Delta_m})^4$.

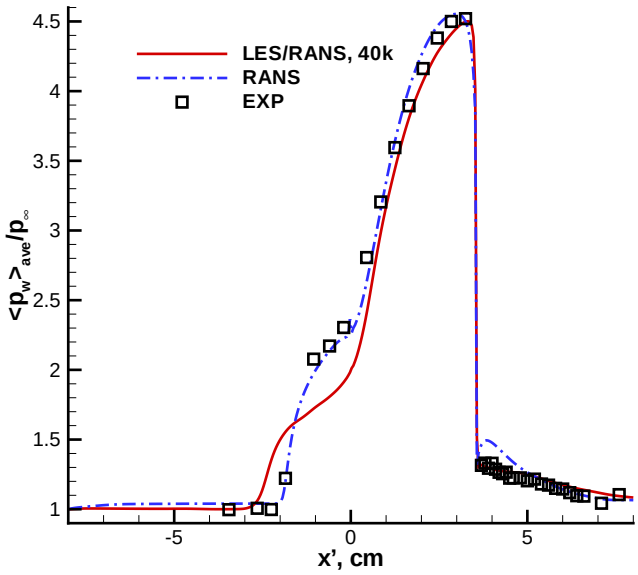

Figure 6.20: 25 Ramp: Comparison of wall pressure distribution, $\Gamma_1 = \tanh(\frac{l_\epsilon}{5\Delta_m})^4$.

6.2.2 Γ_1 *vs* Γ_2 on coarse grid

As discussed earlier, the small LES region might be the reason for the somewhat poor prediction of separation and the skin friction in the recovery region. In order to get a larger LES zone to improve the prediction in the separation region and the recovery region, Δ_m is replaced by Δ_v, but $\alpha_1 = 5$ remains unchanged. In this case, $\Gamma_2 \geq \Gamma_1$, as is seen in Figure 6.21.

Figure 6.22 and Figure 6.23 compare the the mean skin friction and mean wall pressure, respectively. The skin friction results show that streamwise size of the separation zone has been improved by using Γ_2, although it is still not better than RANS solution. This can be also found from the wall pressure distribution. But the wall pressure rise in Γ_2 case is not as rapid as the RANS result. This indicates the thickness of separation zone is not

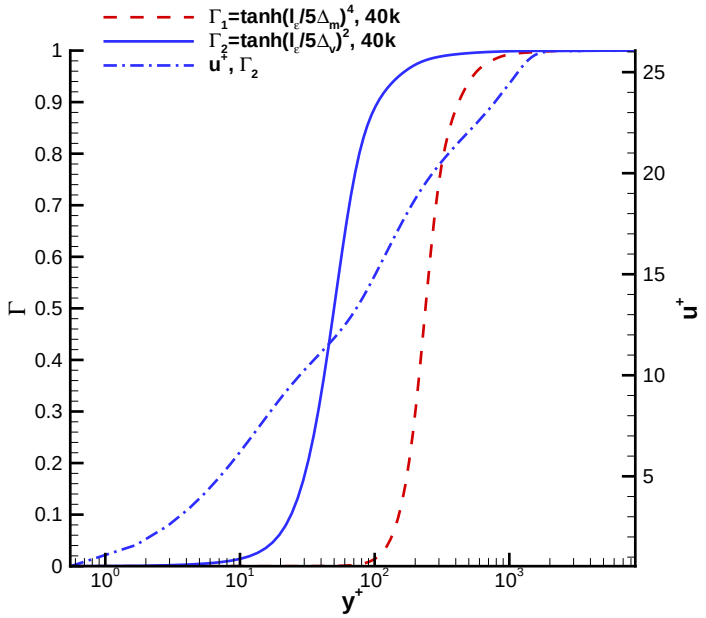

Figure 6.21: 25 Ramp: Blending function profiles on recycle-plane, Γ_1 *vs* Γ_2.

well-predicted.

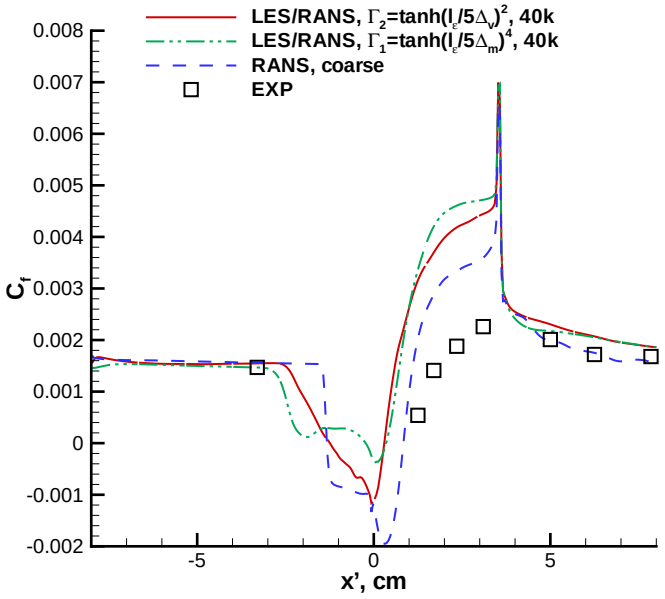

Figure 6.22: 25 Ramp: Skin friction distribution, Γ_1 *vs* Γ_2.

Comparison of the mean eddy viscosity distribution is shown in Figure 6.24. The hybrid

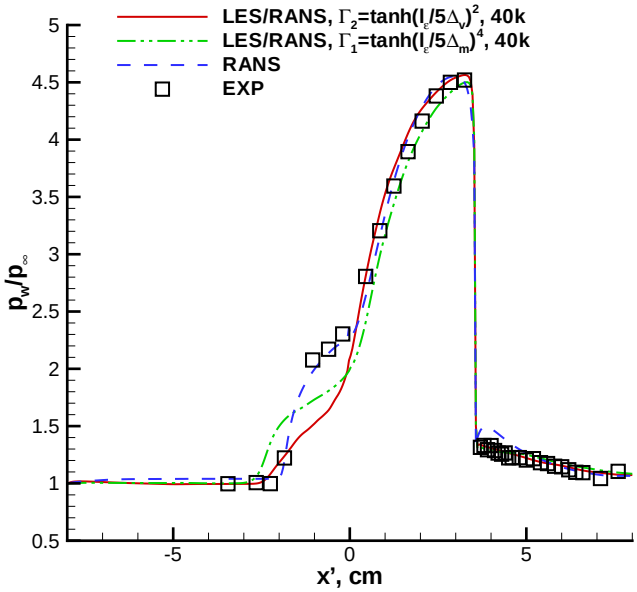

Figure 6.23: 25 Ramp: Wall pressure distribution, Γ_1 *vs* Γ_2.

scheme using Γ_1 is characterized by much larger eddy viscosity than that with Γ_2.

Figure 6.25 compares the mean axial velocity profile at different stations, where y' stands for $y - y_{wall}$.

The velocity in Figure 6.25 are the absolute value of u-component nondimensionalized by the edge velocity from the experimental measurements. The profiles in the separation region show that both hybrid schemes can not reproduce the experimental data. However, in the Γ_2 scheme, where the LES region is larger, the inner backflow structure is resolved in two stations upstream of the compression corner, while Γ_1 scheme does not show this structure in velocity profiles. The backflow size and the peak of backflow velocity predicted by Γ_2 scheme are smaller than the RANS results. This reduced backflow thickness is consistent with the slow pressure rise shown earlier.

Comparing Γ_1 with Γ_2 case, because the initial separation shock wave extends further

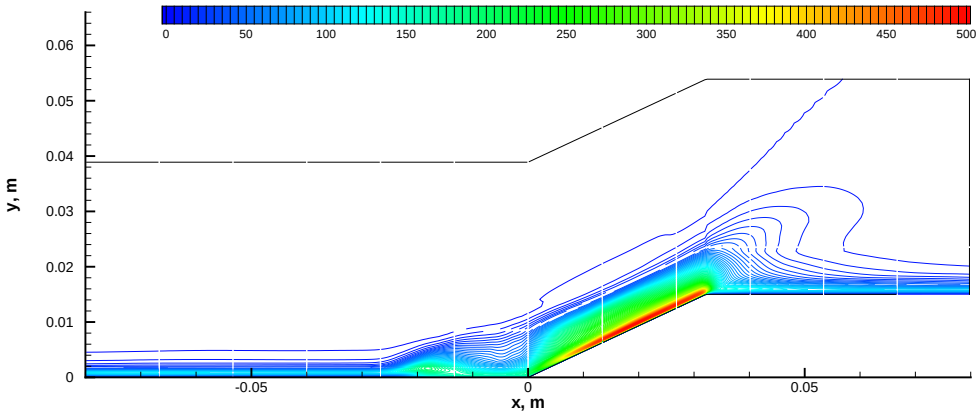

(a) Γ_1, μ_t/μ_∞

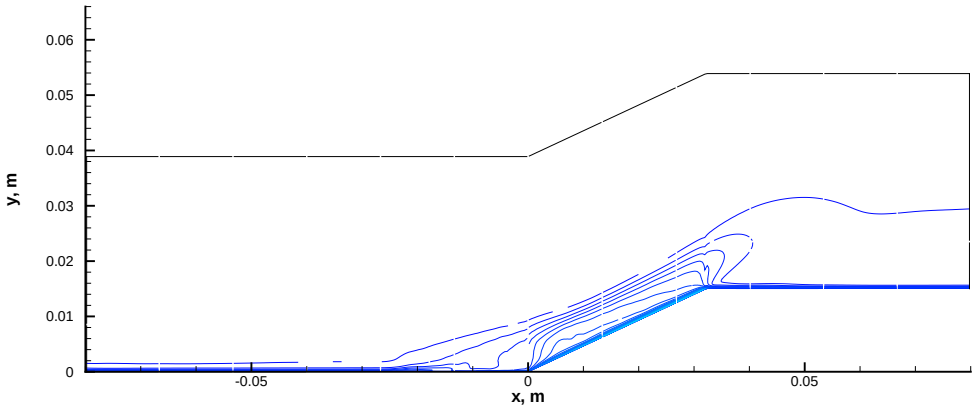

(b) Γ_2, μ_t/μ_∞

Figure 6.24: 25 Ramp: Mean eddy viscosity distribution, Γ_1 *vs* Γ_2.

upstream, the boundary layer of Γ_1 is thicker than that of Γ_2, and therefore the wall pressure level of Γ_1 around the compression corner is higher than that of Γ_2, as shown in Figure 6.23.

At the station downstream of the corner($x' = 0.5\ cm$), neither of hybrid schemes is able to predict the backflow, whereas RANS solution predicts this structure, although the size is not as large as experimental measurements.

In the recovery region, Figure 6.25b shows that the the hybrid schemes do a much better

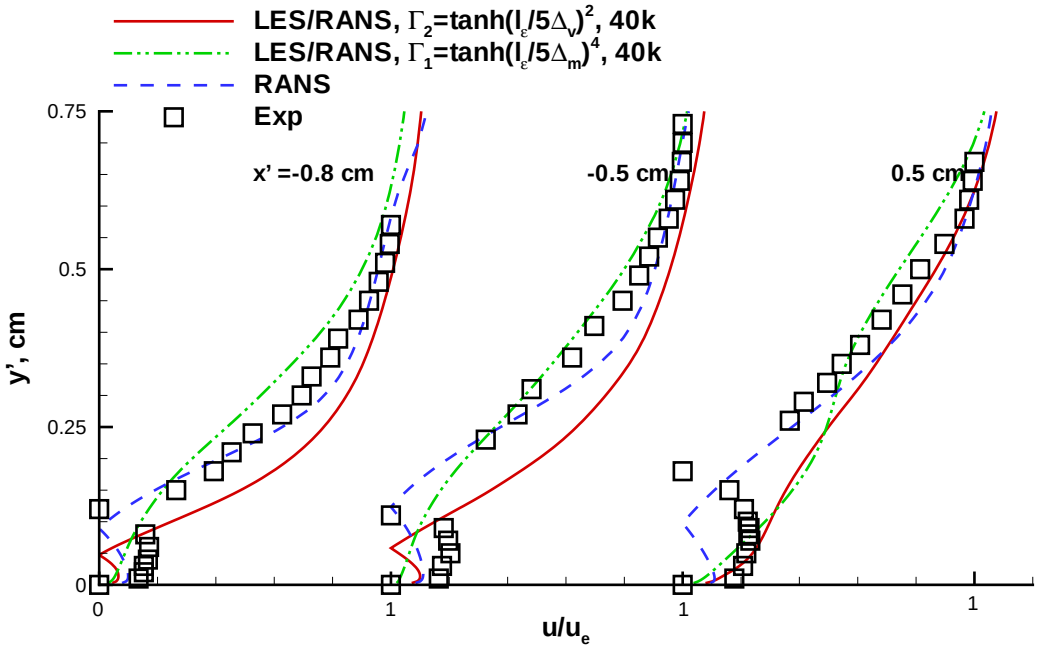

(a) Separation region

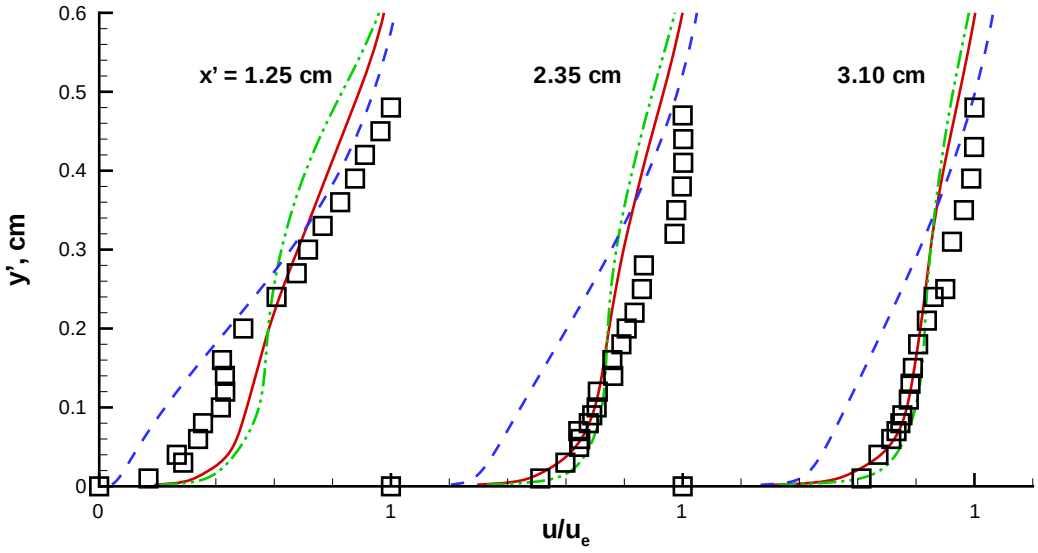

(b) Recovery region

Figure 6.25: 25 Ramp: Comparison of velocity profiles, Γ_1 *vs* Γ_2.

job than the RANS solution in the near-wall region. This is similar to what Fan found[33]. In the outer region of the boundary-layer, both LES/RANS hybrid schemes have similar behavior, and underpredict the velocity.

6.2.3 Effect of α_1 on Γ_2 scheme

Once the RANS model and the grid have been decided, the model constant α_1 determines the behavior of the blending function. Large α_1 will delay the transition from RANS to LES, and therefore has large RANS region, as shown in Figure 6.26. One side effect of this is that the maximum of blending function can not reach 1.0, which means a complete LES region does not exist far away from the wall.

In the case of $\alpha_1 = 5$, the transition between the RANS region and the LES region takes place between $y^+ = 10$ and $y^+ = 200$. This $y+$ range contains the buffer zone between viscous sublayer and the log law layer. Therefore, the mean velocity profile of $\alpha_1 = 5.0$ is not calculated as well as that of $\alpha_1 = 10$. The log law layer is better recovered by the case where $\alpha_1 = 10$, as presented in Figure 6.27.

As a result of increasing α_1, the Γ_2 with $\alpha_1 = 10.0$ predicts smaller separation zone around the corner, as shown in Figure 6.28. However, the initial separation shock wave position, which is also shown in the wall pressure distribution, Figure 6.29, is slightly affected.

Due to the larger RANS region, $\alpha_1 = 10$ case gives even higher skin friction than $\alpha_1 = 5$ on the ramp surface.

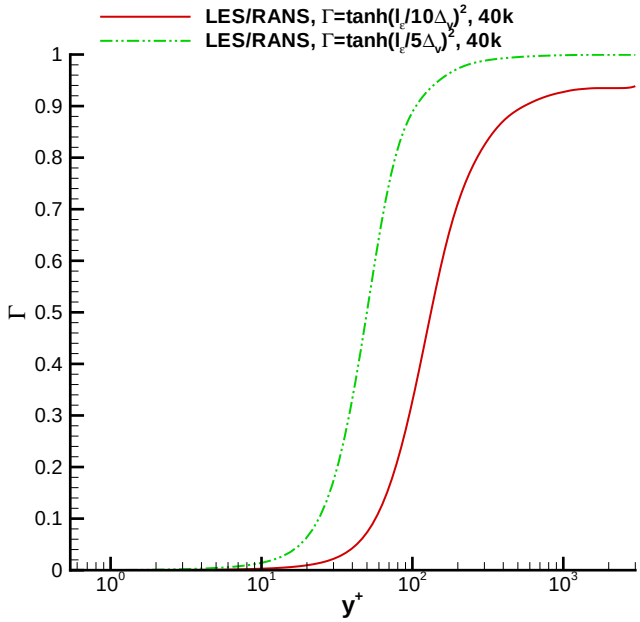

Figure 6.26: 25 Ramp: Profiles of blending function on recycle-plane, Γ_2.

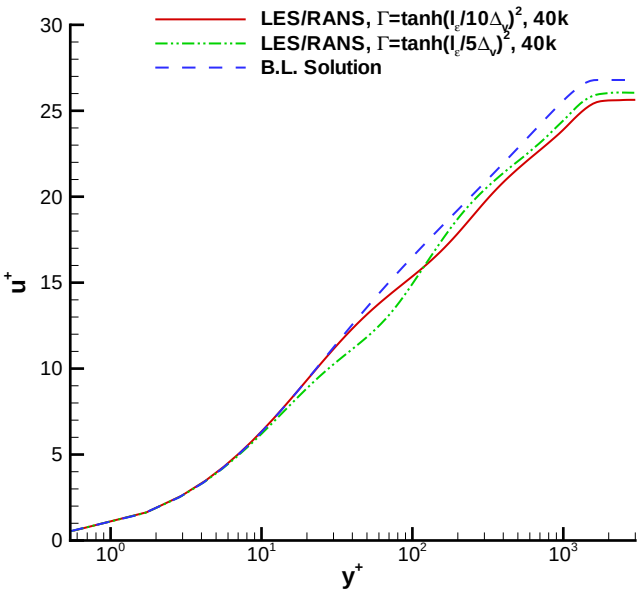

Figure 6.27: 25 Ramp: Mean velocity profiles on recycle-plane, Γ_2.

Figure 6.30 compares the mean axial velocity profile in different stations. As α_1 increases, the hybrid scheme has the trend to improve the velocity prediction in the outer

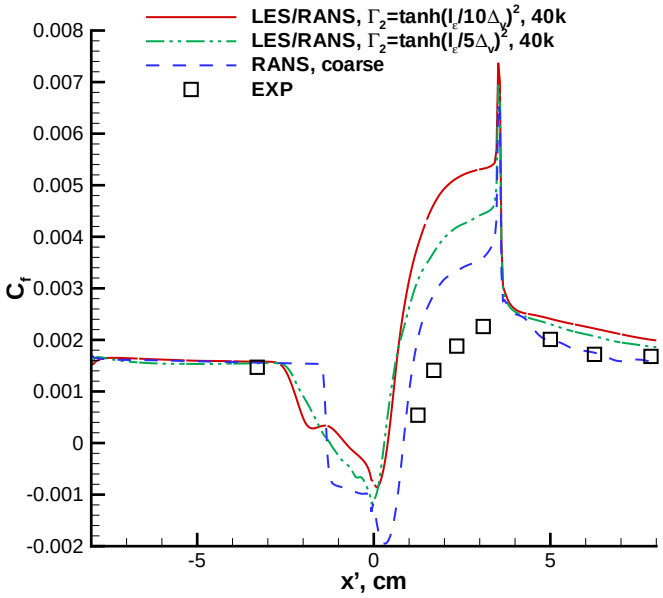

Figure 6.28: 25 Ramp: Skin friction distribution, Γ_2.

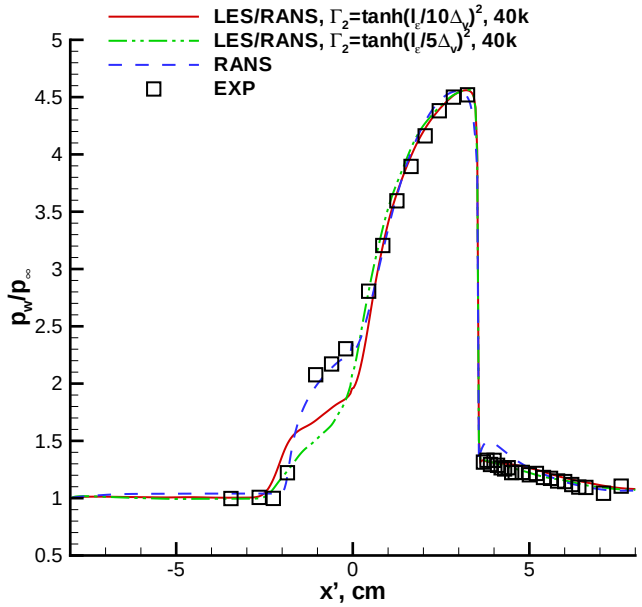

Figure 6.29: 25 Ramp: Wall pressure distribution, Γ_2.

region at the station upstream of the compression corner(Figure 6.30a) by matching the experimental data and increasing the boundary layer thickness. The latter leads to the higher

pressure rise in the separation region, as shown in Figure 6.29. However, it loses the back-flow structure in the inner region. In the recovery region, both Γ_2 schemes give similar results: similar profile shape at $x' = 1.25\ cm$ and good prediction in the near-wall region at the remaining stations.

6.2.4 Grid Refinement Study

Note that both Γ_1 and Γ_2 are grid dependent. Their behavior on different grids should be investigated. On the other hand, comparisons of skin friction between different hybrid schemes indicate that hybrid schemes always generate large skin friction, which is not consistent with their smaller eddy viscosity when compared to the RANS solution. One reason behind this might be grid related. Therefore, above two factors necessitate the grid refinement study. Moreover, the grid-independent blending function, Γ_3, must be evaluated using different grid sizes.

The 2D RANS solutions on the two grids are compared in Figure 6.31. Both grids yield essentially identical RANS results, except for a slightly larger separation zone in the refined grid. This might be due to the smaller numerical dissipation associated with the fine mesh.

In this section, the time-averaged data on refined grid are collected from No. 20k to No. 40k iteration. The RANS solutions to which the LES/RANS results are compared are those obtained from the refined grid.

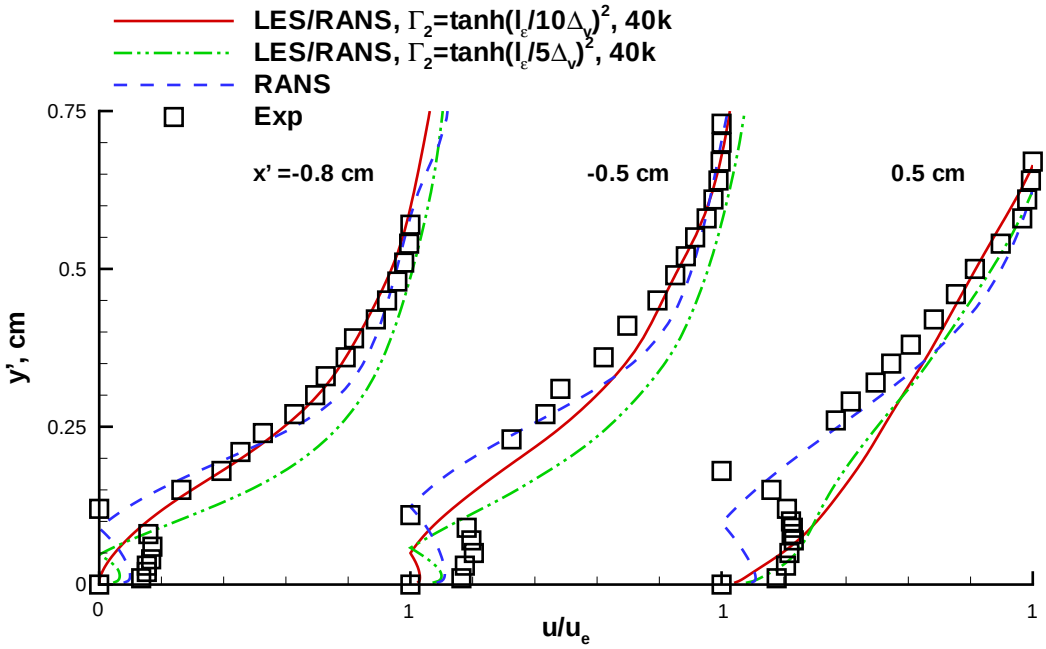

(a) Separation region

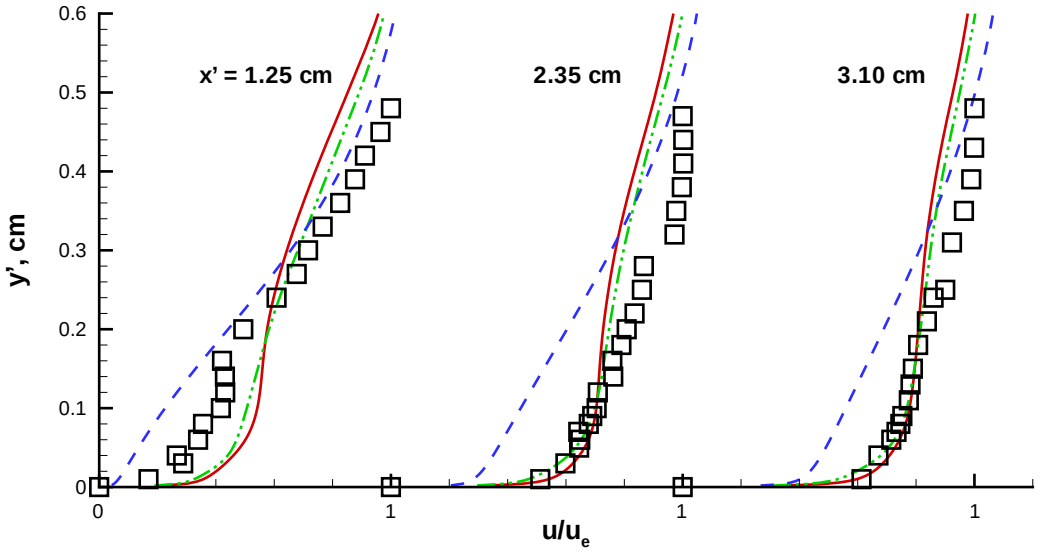

(b) Recovery region

Figure 6.30: 25 Ramp: Comparison of velocity profiles, Γ_2

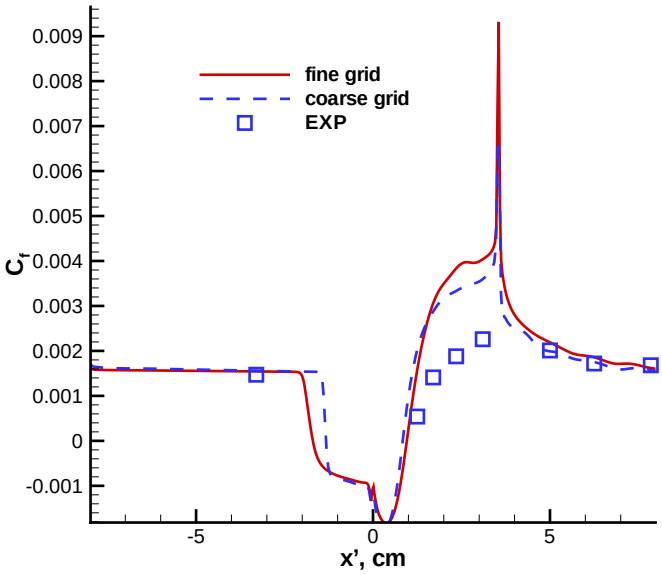

(a) Skin friction distribution.

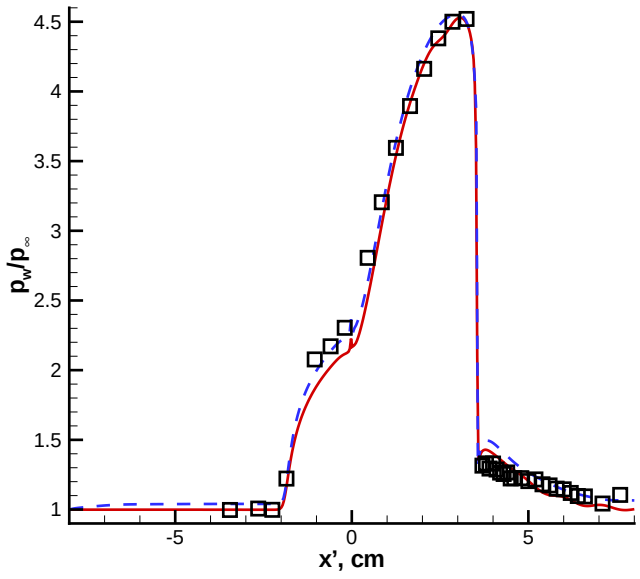

(b) Wall pressure distribution.

Figure 6.31: 25 Ramp: Comparison of 2D RANS solutions

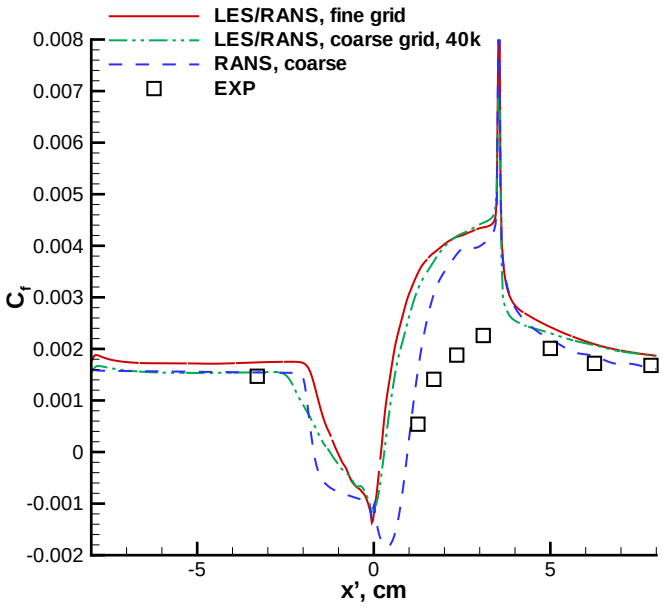

Figure 6.32: 25 Ramp: Skin friction distribution, $\Gamma_2 = \tanh\left(\frac{l_\epsilon}{5\Delta_v}\right)^2$.

Γ_2 scheme

On both grids, $\Gamma_2 = \tanh\left(\frac{l_\epsilon}{5\Delta_v}\right)^2$ is used to conduct the numerical experiments. On the flat plate ahead of the compression corner, Figure 6.32 shows that higher skin friction is predicted on the fine mesh, which means the inflow turbulent boundary layer is more energetic. As a result of this, the separation zone shrinks on the refined mesh. In the remaining region, both skin friction distributions are comparable. The evidence of the increasing energy among the boundary layer can be found from the *RMS* mass flux fluctuations on the recycle-plane (Figure 6.33). In most of the inner region of the boundary layer, the *RMS* value on the refined grid is greater than that from the coarse mesh. As shown in Figure 6.34, the grid refinement tends to increase the LES region using Γ_2 scheme. Thus, increasing of LES region will also enhance the turbulence fluctuations.

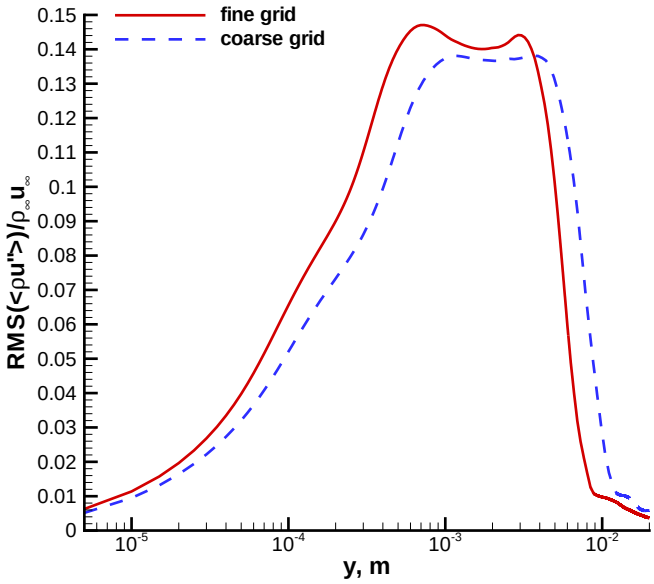

Figure 6.33: 25 Ramp: *RMS* mass flow fluctuation profiles, $\Gamma_2 = \tanh\left(\frac{l_\epsilon}{5\Delta_v}\right)^2$, on recycle-plane.

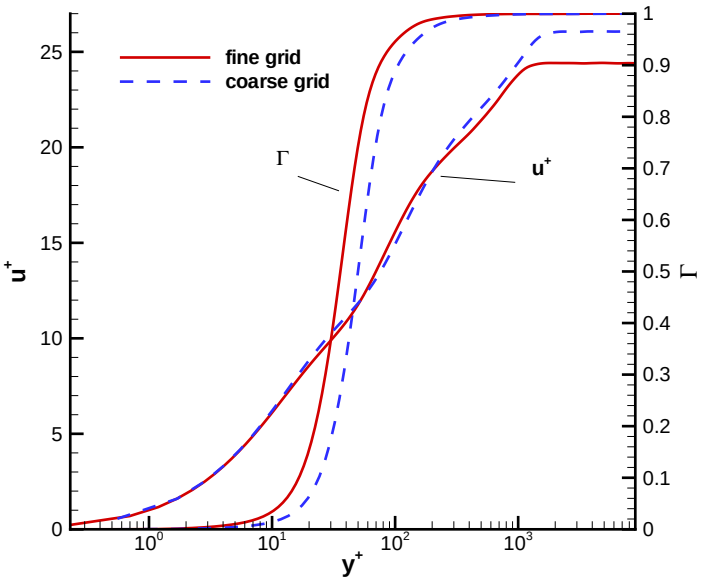

Figure 6.34: 25 Ramp: Blend function profiles and mean velocity profiles, $\Gamma_2 = \tanh\left(\frac{l_\epsilon}{5\Delta_v}\right)^2$, on recycle-plane.

The skin friction results also indicate that not too much improvement results from grid refinement. The mean velocity profiles are presented in Figure 6.35. In the separation region, the results from refined grid are worse than those from coarse mesh: the size of the backflow region becomes smaller, and the velocities above the backflow region are greater than those from coarse grid and are further away from the experimental data. This behavior is a result of the higher energy level in the boundary layer.

Thus, the blending function Γ_2 is sensitive to the grid refinement. It appears that α_1 is grid dependent.

The results in the recovery region are somewhat encouraging. The velocity profiles from the refined grid match the entire experimental data very well. Significant improvement occurs in the outer region of the boundary layer.

Γ_3 scheme

Γ_3 is defined as a blending function without explicit grid dependence. This independence of grid is supported by the results from skin friction distribution(Figure 6.36) and the wall pressure distribution(Figure 6.37).

The most persuasive results are the mean velocity profile and the blending function profile on the recycle-plane, which are presented in Figure 6.38. Compared with the previous blending functions, this one recovers the perfect log layer in both grids. There is no "grey region" phenomenon! Two coincident blending function (in transient region) profiles reflect the property of grid independence. The smaller value of blending function in the outer region on the refined mesh might be a result of smaller size of resolved eddies.

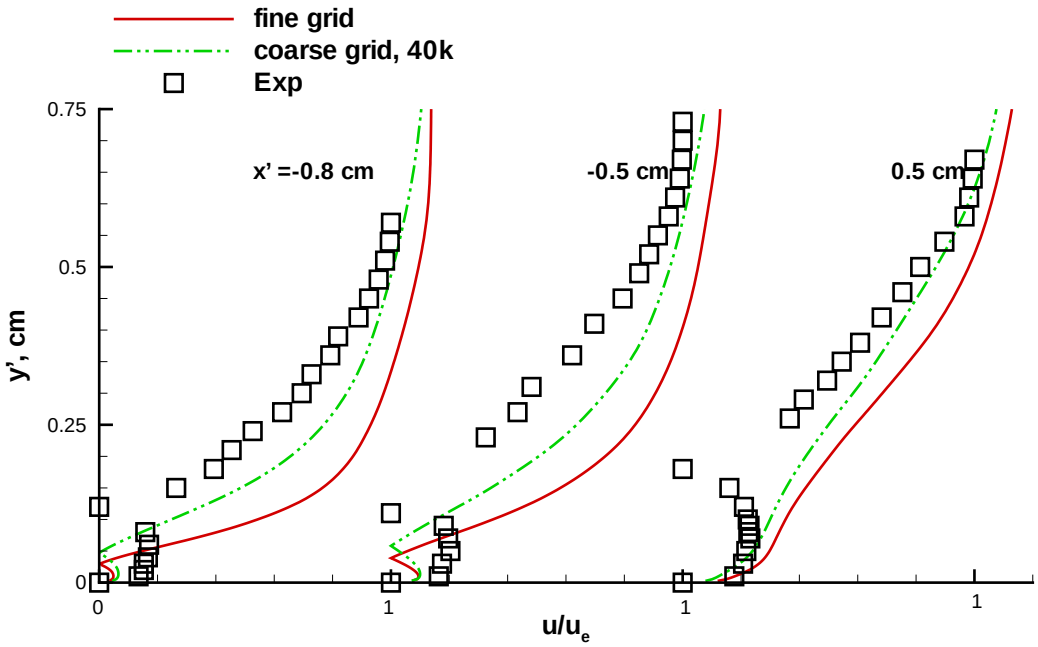

(a) Separation region

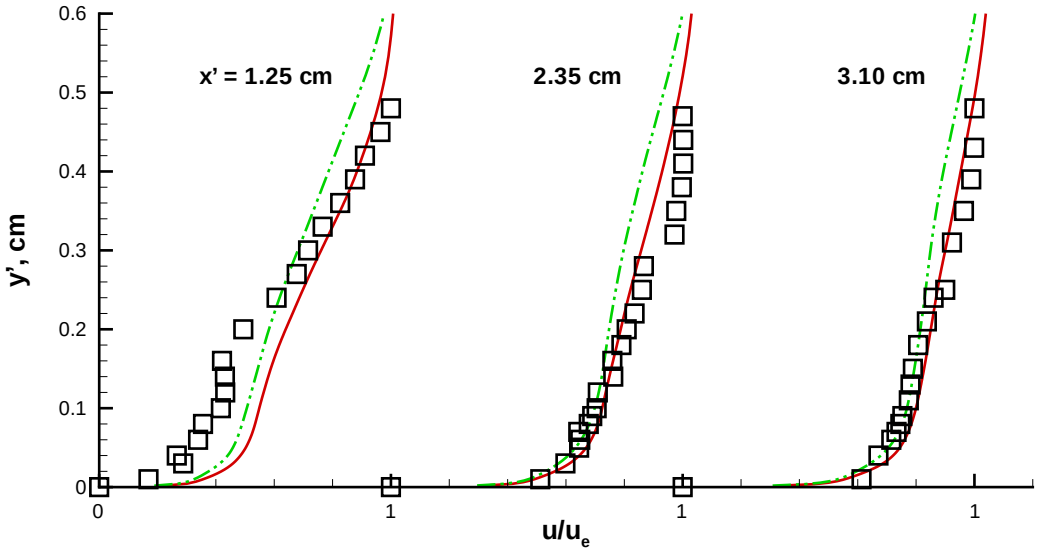

(b) Recovery region

Figure 6.35: 25 Ramp: Comparison of velocity profiles, $\Gamma_2 = \tanh\left(\frac{l_\epsilon}{5\Delta_v}\right)^2$.

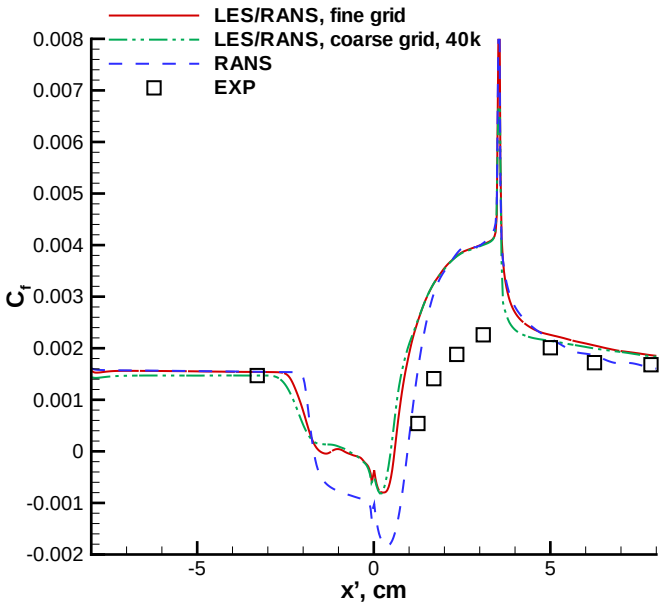

Figure 6.36: 25 Ramp: Skin friction distribution, $\Gamma_3 = \tanh\left(\frac{l_s}{25\lambda}\right)^2$.

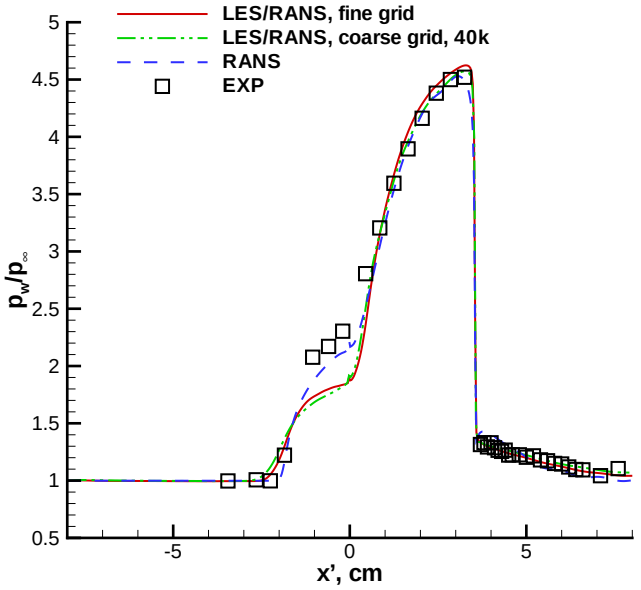

Figure 6.37: 25 Ramp: Wall pressure distribution, $\Gamma_3 = \tanh\left(\frac{l_s}{25\lambda}\right)^2$.

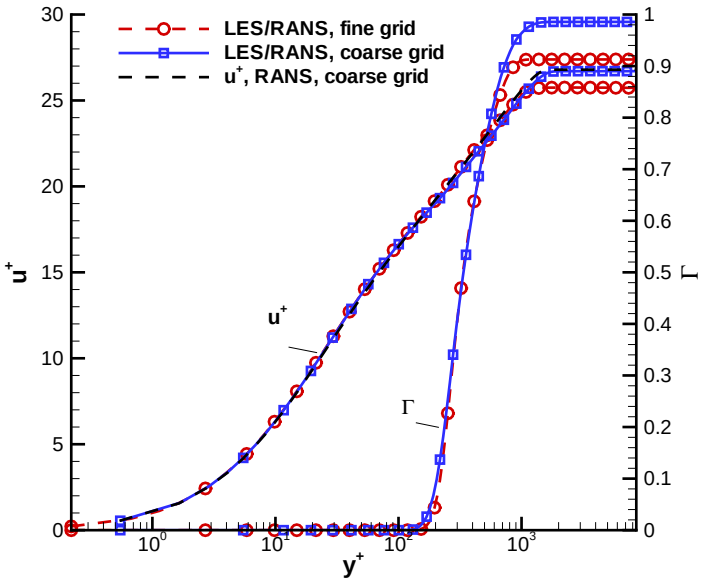

Figure 6.38: 25 Ramp: Blending function profiles, $\Gamma_3 = \tanh\left(\frac{l_s}{25\lambda}\right)^2$.

But the good performance of Γ_3 scheme on the flat plate section is not a sufficient condition for improve downstream prediction, as illustrated in Figure 6.39. In the stations upstream of the corner, this scheme can not resolve the backflow structure as well as Γ_2 scheme does. And at the station immediately downstream of the corner, this scheme, like the other schemes, cannot reproduce the backflow either. In the recovery region, all the velocity profiles are close to the experimental data. Likewise, the hybrid scheme on the refined mesh works better in the outer region.

6.3 20 Ramp Flow

In this flow, $\Gamma_3 = \tanh\left(\frac{l_s}{25\lambda}\right)^2$ is employed. The instantaneous streamwise velocity on the x-y plane is presented in Figure 6.40. The turbulence structure in the incoming flow,

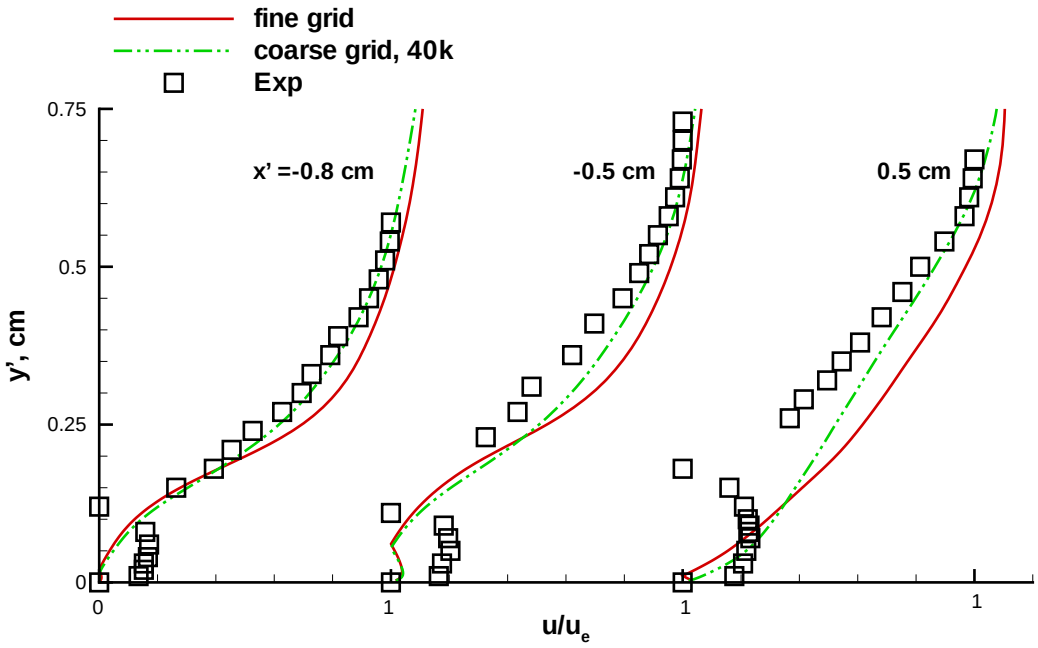

(a) Separation region

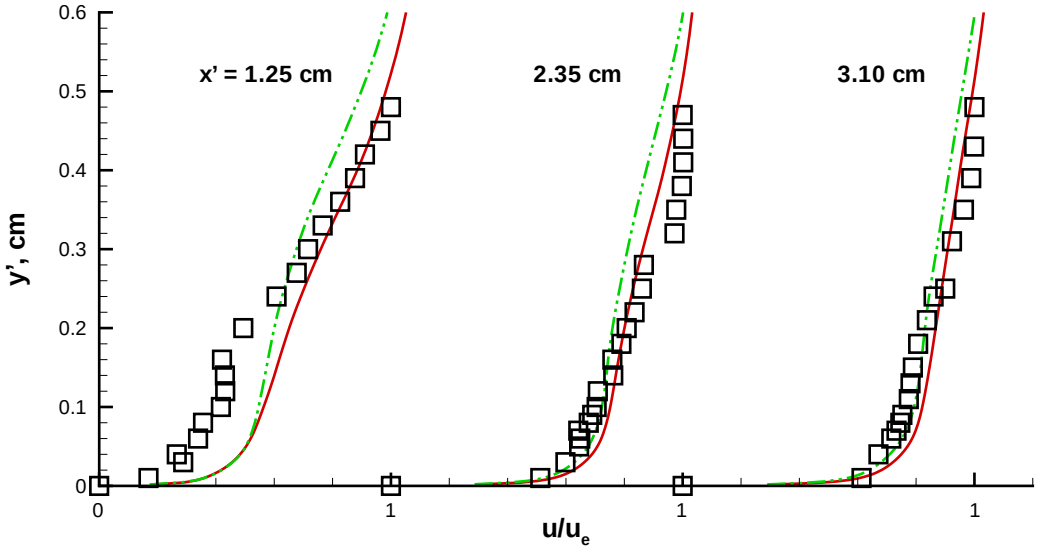

(b) Recovery region

Figure 6.39: 25 Ramp: Comparison of velocity profiles, $\Gamma_3 = \tanh\left(\frac{l_s}{25\lambda}\right)^2$.

generated by the rescaling-reintroducing method, is visible. The typical structures of this flow include the separation bubble around the corner, and the embedded shock emanating from the flow reattachment.

The statistical information were collected for an additional 12k iterations, after 47k iterations from the combined initial solution of LES/RANS on the flat plate and RANS on the ramp.

Figure 6.42 compares the skin friction from hybrid scheme with the experimental data, the RANS solution and Fan's SST hybrid scheme solution[33], which is calculated by using current rescaling-reintroducing method to generate the inflow turbulence. In this and subsequent figures, x' is defined along the surface with the origin at the ramp apex, and y' is defined as the normal distance to the wall.

Compared with RANS result, current hybrid scheme has a smaller size of separation, which is comparable to Fan's results. But it is still larger than the experimental measurement. As far as the drop in skin friction is concerned, the decrease of C_f in current hybrid scheme starts farther downstream than Fan's results, which indicates a delayed initial separation shock wave. However, the position of the separation shock wave, $x' \approx 4.0\ cm$, is still upstream of the experimental one. The initial rise of wall pressure in Figure 6.41 also reveals this situation.

In the incoming boundary layer, current scheme gives the smallest skin friction, which implies the LES region is too large. Figure 6.43 shows the profile of blending function on the recycle-plane. The transition from the RANS region to the LES region is at $y^+ = 100$, which is almost at the lower boundary of log layer. If the switch between two regions can

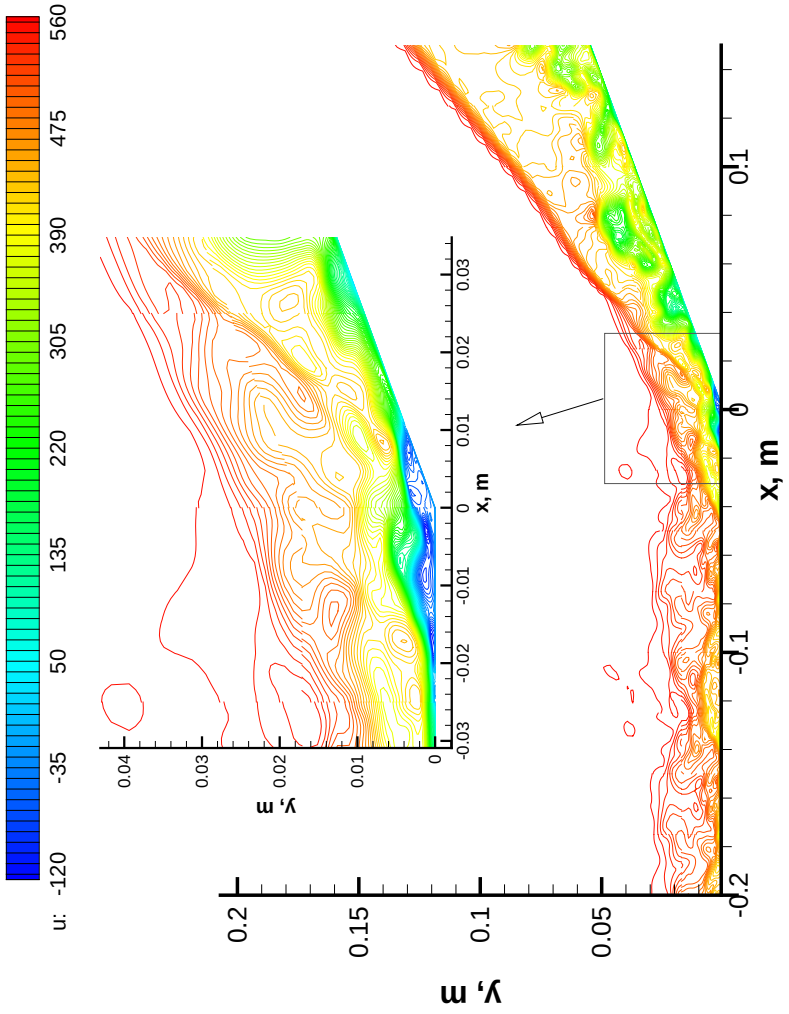

Figure 6.40: 20 Ramp: Instantaneous streamwise velocity(u) distribution.

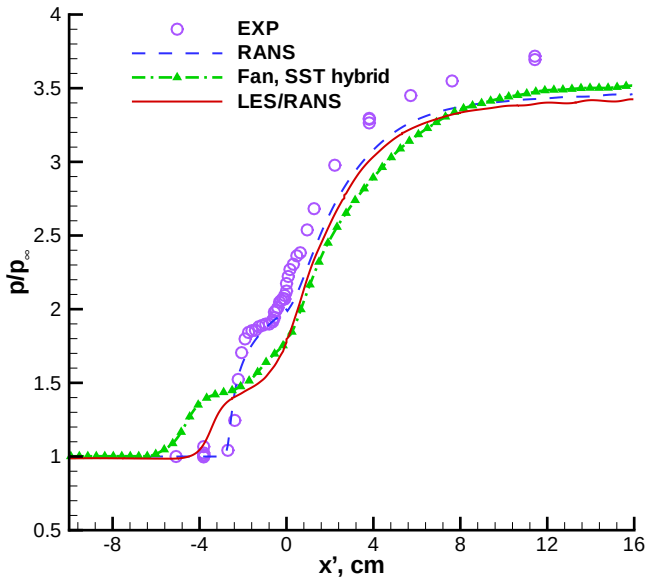

Figure 6.41: 20 Ramp: Wall pressure distribution.

be moved farther away from the wall, then the RANS region can become larger and the skin friction prediction can be improved. And the initial separation shock wave can be pushed further downstream.

Figure 6.44 and Figure 6.45 present the velocity profiles at a series of locations. The velocity in these two figures is the component parallel to the wall, divided by the measured edge velocity. At $x' = -3.81\ cm$, current hybrid scheme matches the experimental very well. However, due to the inaccurate initial separation shock wave, the velocity is under-predicted in the near-wall region.

Because of the improved prediction of separation shock wave position over Fan's scheme, Γ_3 scheme gives better result around the corner. This also leads to significant improvements in the recovery region. At all five stations, the solutions from Γ_3 scheme coincide with the experimental data, in both inner and outer regions.

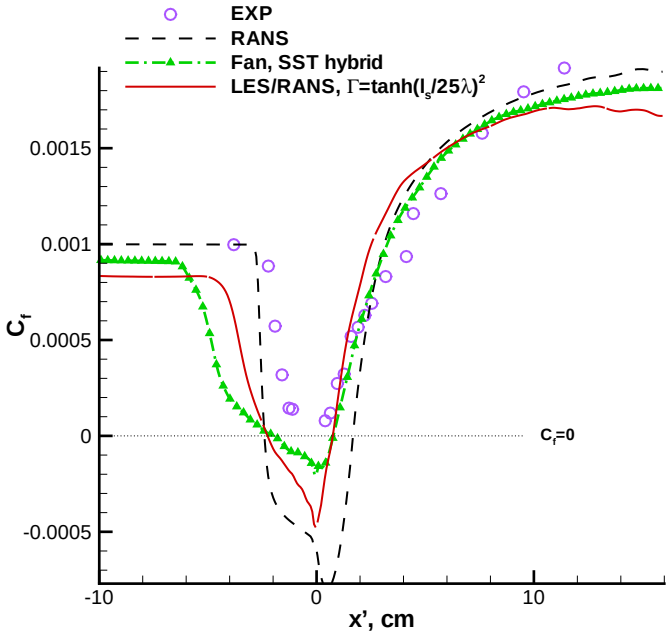

Figure 6.42: 20 Ramp: Skin friction distribution.

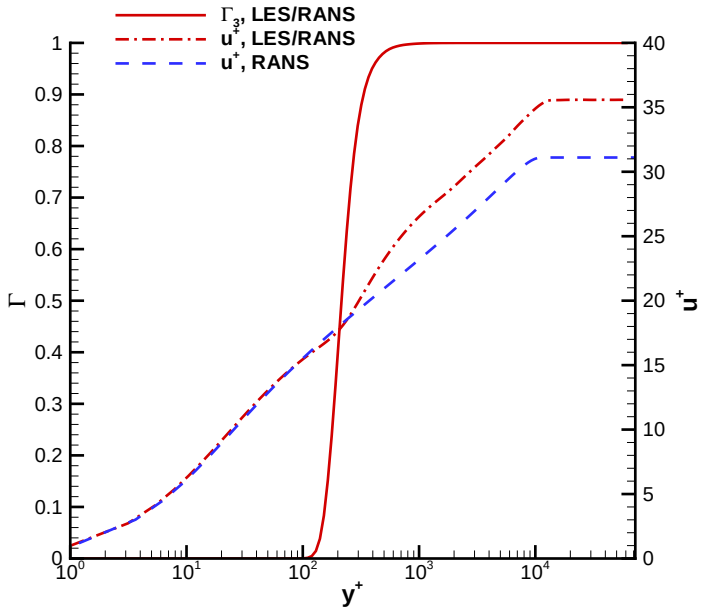

Figure 6.43: 20 Ramp: Profiles of blending function and mean velocity.

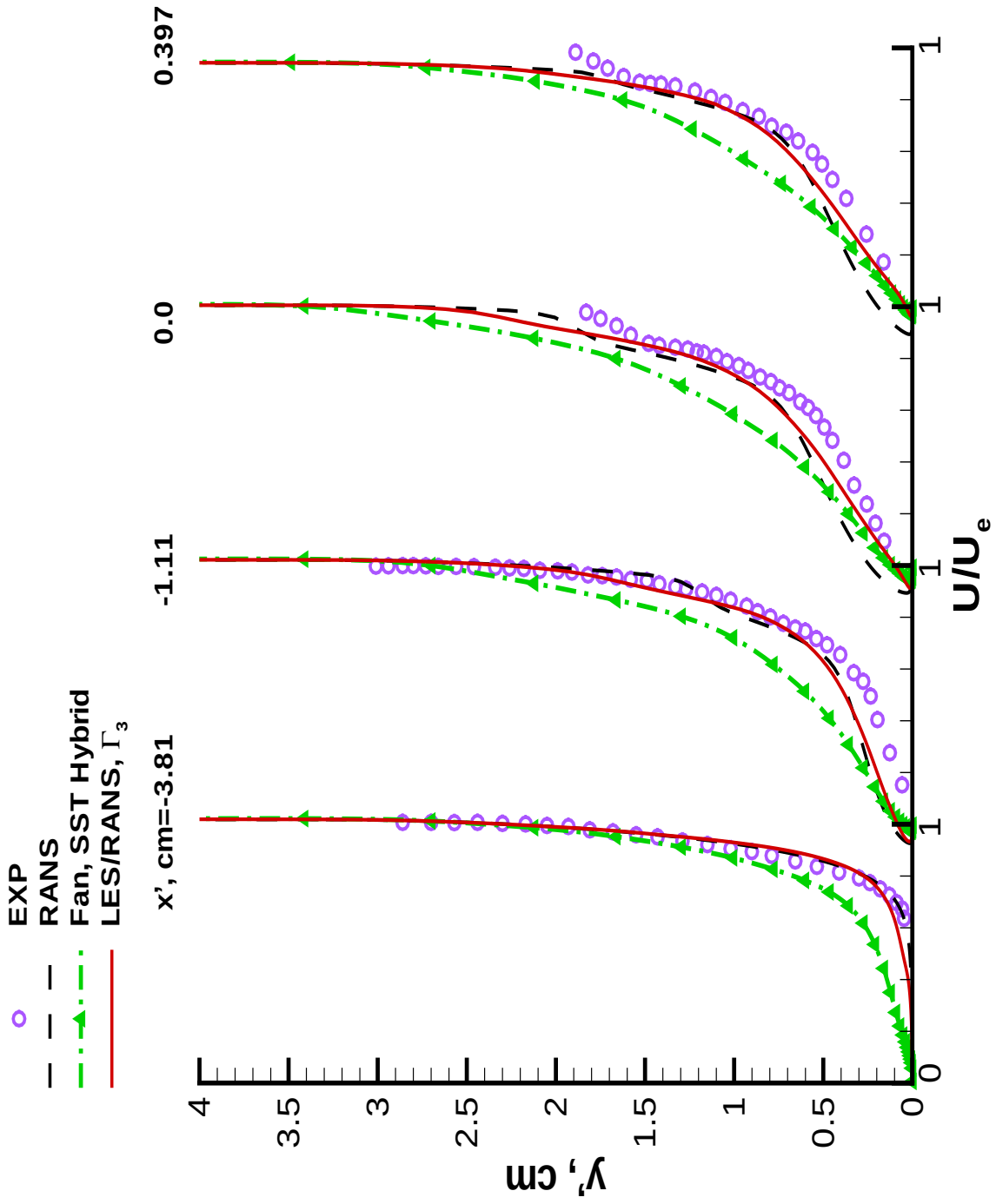

Figure 6.44: 20 Ramp: Velocity profiles in the vicinity of ramp apex.

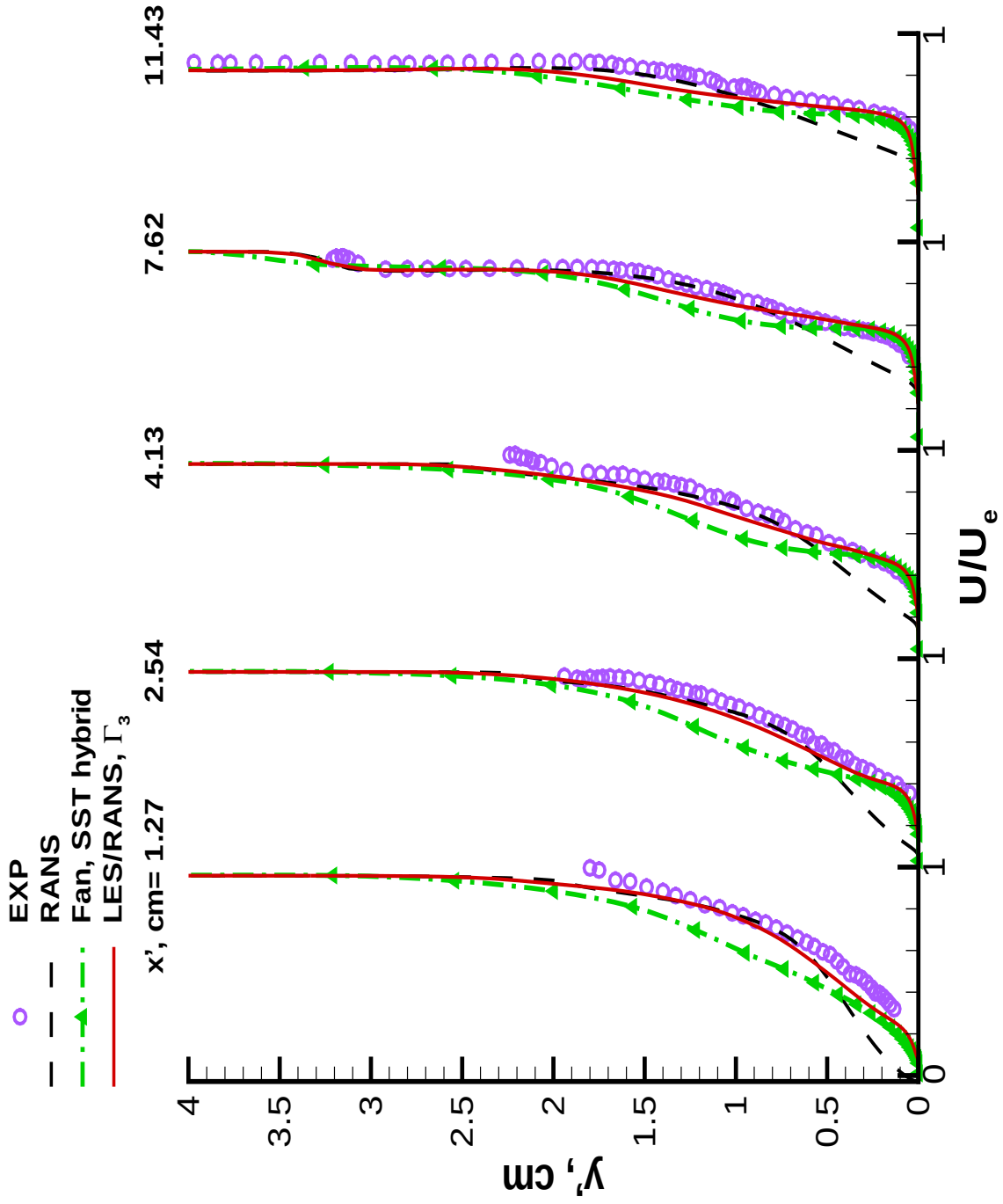

Figure 6.45: 20 Ramp: Velocity profiles in recovery region.

Chapter 7

Conclusions

In this study, the rescaling-reintroducing method for generating turbulent inflow condition has been extended to the LES/RANS hybrid schemes. By using monotonic blending functions, the modified rescaling-reintroducing method is capable of generating turbulence structures. In the meantime, it is able to maintain the desired mean inflow profiles.

Using this method, three wall-distance free LES/RANS hybrid schemes have been tested on Zheltovodov's 25 deg ramp and Settles' 20 deg ramp problems. To prevent the initial growth of separation bubble when the initial flow is obtained from a RANS solution, a special starting procedure has been implemented. Through this procedure, the fully developed turbulent inflow over flat plate is combined with the downstream RANS solution to initialize the whole flow field for ramp problems. The application of the procedure shows that it can effectively keep initial separation shock wave from reaching the recycle-plane, and therefore the inflow generation section can work properly without the downstream influence.

The tests on 25 deg ramp case demonstrate that the Γ_2 scheme can produce better backflow structure upstream of the compression corner than other hybrid schemes. And via the grid refinement study, Γ_3 shows its grid independence and recovers the smooth and continuous log law layer profile. However, all three hybrid schemes suffer from poor predictions

in the separation region, which include inaccurate backflow structure and smaller separation size. Nevertheless, in the recovery region, all hybrid schemes do show improvements over the RANS simulation, especially in the near-wall region. And the grid refinement extends the improvement to the outer region.

In the simulation of 20 deg ramp flow, comprehensive improvements over RANS and Fan's hybrid scheme are obtained using Γ_3 scheme. In both the separation region and the recovery region, Γ_3 scheme well predicts the velocity profiles in the near-wall region and in the outer region. By adjusting the model constant, it is hopeful to get further improvement in the incoming flow and in the positioning of initial separation shock wave.

Comparing the inflow boundary layer thickness and the grid size used in these two similar experimental configurations, the grid for 20 deg ramp case is relatively finer than the other one. And based on the observation from the grid refinement study in 25 deg ramp case, current LES/RANS hybrid schemes, or Γ_3 scheme if not all of them, are likely to replace RANS and become an effective tool to simulate shock wave / boundary layer interaction problems on "appropriately" fine mesh.

List of References

[1] Pope, S. B., *Turbulent Flows*, Cambridge University Press, 2000.

[2] Moin, P. and Mahesh, K., "Direct Numerical Simulation: A Tool in Turbulence Research," *Annu. Rev. Fluid Mech.*, Vol. 30, 1998, pp. 539–578.

[3] Wilcox, D. C., *Turbulence Modeling for CFD*, DCW Industries, 2nd ed., 1998.

[4] Chapman, D. R., "Computational Aerodynamics Development and Outlook," *AIAA Journal*, Vol. 17, 1979, pp. 1293–1313.

[5] Piomelli, U. and Balaras, E., "Wall-Layer Models for Large-Eddy Simulations," *Annual Review of Fluid Mechanics*, Vol. 34, 2002, pp. 349–374.

[6] Deardorff, J. W., "A Numerical Study of Three-Dimensional Turbulent Channel Flow at Large Reynolds Numbers," *Journal of Fluid Mechanics*, Vol. 41, 1970, pp. 453–480.

[7] Schumann, U., "Subgrid Scale Model for Finite Difference Simulations in Plane Channels and Annuli." *J. Comp. Phys.*, Vol. 18, 1975, pp. 376–404.

[8] Piomelli, U., Moin, P., Ferziger, J. H., and Kim, J., "New Approximate Boundary Conditions for Large-Eddy Simulations of Wall-Bounded Flows," *Physics of Fluids A*, Vol. 1, 1989, pp. 1061–1068.

[9] Balaras, E. and Benocci, C., "Subgrid-Scale Models in Finite-Difference Simulations of Complex Wallbounded Flows," *AGARD CP 551*, 1994, pp. 2.1–2.5.

[10] Balaras, E., Benocci, C., and Piomelli, U., "Two-Layer Approximate Boundary Conditions for Large-Eddy Simulations," *AIAA journal*, Vol. 34, pp. 1111–1119.

[11] Steger, J. L., Dougherty, F. C., and Benek, J. A., "A Chimera Gird Scheme," *Advances in Gird Generation*, edited by K. N. Ghia and U. Ghia, Vol. 5 of *FED*, ASME, 1983, pp. 59–69.

[12] Spalart, P. R., Jou, W.-H., Strelets, M., and Allmaras, S., "Comments on the Feasibility of LES for Wings and on a Hybrid RANS/LES Approach," *Advances in DNS/LES*, edited by C. Liu and Z. Liu, First AFOSR Int. Conf. on DNS/LES, Aug 4-8, Ruston, LA., Greyden Press, Columbus, OH, 1997, pp. 137–147.

[13] Cabot, W. and Moin, P., "Approximate Wall Boundary Conditions in the Large-Eddy Simulation of High Reynolds Number Flow," *Flow, Turbulence and Combustion*, Vol. 63, 1999, pp. 269–291.

[14] Spalart, P. R. and Allmaras, S. R., "A One-Equation Turbulence Model for Aerodynamic Flows," *La Recherche Aérospatiale*, , No. 1, 1994, pp. 5–21.

[15] Smagorinsky, J., "General Circulation Experiments with the Primitive Equations. I. The Basic Experiment," *Mon. Weather Rev.*, Vol. 91, 1963, pp. 99–164.

[16] Spalart, P. R., "Young-Person's Guide to Detached-Eddy Simulation Grids," NASA CR-2001-211032, 2001.

[17] Nikitin, N. V., Nicoud, F., Wasistho, B., Squires, K. D., and Spalart, P. R., "An Approach to Wall Modeling in Large-Eddy Simulations," *Physics of Fluids*, Vol. 12, No. 7, July 2000, pp. 1629–1632.

[18] Travin, A., Shur, M., Strelets, M., and Spalart, P. R., "Detached-Eddy Simulations Past a Circle Cylinder," *Flow, Turbulence and Combustion*, Vol. 63, 1999, pp. 293–313.

[19] Squires, K. D., Forsythe, J. R., Motton, S. A., Strang, W. Z., Wurtzler, K. E., Tomaro, R. F., Grismer, M. J., and Spalart, P. R., "Progress on Detached-Eddy Simulation of Massively Separated Flows," AIAA Paper 2002-1021, Jan 2002.

[20] Strelets, M., "Detached Eddy Simulation of Massively Separated Flows," AIAA Paper 2001-0879, Jan 2001.

[21] Bush, R. and Mani, M., "A Two-Equation Large-Eddy Stress Model for High Sub-Grid Shear," AIAA Paper 2001-2561, June 2001.

[22] Speziale, C. G., "Computing Non-Equilibrium Flows with Time-Dependent RANS and VLES," *Fifteenth International Conference on Numerical Methods in Fluid Dynamics: Proceedings of the conference held in Monterey, CA, USA, 24-28 June 1996*, edited by P. Kutler, J. Flores, and J.-J. Chattot, No. 490 in Lecture Notes in Physics, Springer, 1997, pp. 123–129, ISBN 3540630546.

[23] Speziale, C. G., "Turbulence Modeling for Time-Dependent RANS and VLES: A Review," *AIAA Journal*, Vol. 36, No. 2, February 1998, pp. 173–184.

[24] Arunajatesan, S., Sinha, N., and Menon, S., "Towards Hybrid LES–RANS Computations of Cavity Flowfields," AIAA Paper 2000-0401, Jan 2000.

[25] Arunajatesan, S. and Sinha, N., "Unified Unsteady RANS–LES Simulation of Cavity Flowfields," AIAA Paper 2001-0516, Jan 2001.

[26] Zhang, H.-L., Bachman, C. R., and Fasel, H. F., "Application of New Methodology for Simulations of Complex Turbulent flows," AIAA Paper 2000-2535, June 2000.

[27] Batten, P., Goldberg, U. C., and Chakravarthy, S. R., "Sub-Grid Turbulence Modeling for Unsteady Flow with Acoustic Resonance," AIAA Paper 2000-0473, Jan 2000.

[28] Batten, P., Goldberg, U., and Chakravarthy, S., "LNS – An Approach towards Embedded LES," AIAA Paper 2002-0427, Jan 2002.

[29] Georgiadis, N. J., Iwan, J., Alexander, D., and Reshotko, E., "Development of a Hybrid RANS/LES Method for Compressible Mixing Layer Simulations," AIAA Paper 2001-0289, Jan 2001, [NASA/TM–2001-210762].

[30] Baurle, R. A., Tam, C. J., Edwards, J. R., and Hassan, H. A., "An Assessment of Boundary Treatment and Algorithm Issues on Hybrid RANS/LES Solution Strategy," AIAA Paper 2001-2562, June 2001.

[31] Fan, T. C., Tian, M., Edwards, J. R., Hassan, H. A., and Baurle, R. A., "Validation of a Hybrid Reynolds-Averaged/Large-Eddy Simulation Method for Simulating Cavity Flameholder Configuration," AIAA Paper 2001-2929, June 2001.

[32] Fan, T. C., Xiao, X., Edwards, J. R., Hassan, H. A., and Baurle, R. A., "Hybrid LES/RANS Simulation of a Shock Wave / Boundary Layer Interaction," AIAA Paper 2002-0431, Jan 2002.

[33] Fan, T. C., *Hybrid Reynolds-averaged / Large-Eddy Simulation of Ramp-Cavity and Compression Ramp Flow-fields*, Master's thesis, North Carolina State University, Aug 2002.

[34] Lund, T. S., Wu, X., and Squires, K. D., "Generation of Turbulent Inflow Data for Spatially-Developing Boundary Layer Simulation," *Journal of Computational Physics*, Vol. 140, 1998, pp. 233–258.

[35] Hassan, H. A., "LES Boundary Condition for 3-D Flows," unpublished.

[36] Norris, J. W. and Edwards, J. R., "Large-Eddy Simulation of High-Speed Turbulent Diffusion Flames with Detailed Chemistry," AIAA Paper 1997-0370, Jan 1997.

[37] Le, H. and Moin, P., "Direct Numerical Simulation of Turbulent Flow over a Backward-Facing Step," Report TF-58, Thermosciences Div., Dept. Mech. Eng., Standford University, Standford, CA 94305, 1994.

[38] Le, H., Moin, P., and Kim, J., "Direct Numerical Simulation of Turbulent Flow over a Backward-Facing Step," *Journal of Fluid Mechanics*, Vol. 330, 1997, pp. 349.

[39] Spalart, P. R. and Leonard, A., "Direct Numerical Simulation of Equilibrium Turbulent Boundary Layers," *Proc. 5th Symp. on Turbulent Shear Flows*, Ithaca, NY, 1985.

[40] Urbin, G. and Knight, D., "Large-Eddy Simulation of a Supersonic Boundary Layer Using an Unstructured Grid," *AIAA Journal*, Vol. 39, No. 7, July 2001, pp. 1288–1295.

[41] Comte, P. and Lesieur, M., "Large-Eddy Simulations of Compressible Turbulent Flows," in [57].

[42] Lesieur, M., *Turbulence in Fluids*, Vol. 40 of *Fluid Mechanics and its Applications*, Kluwer Academic Publishers, Boston, 1997.

[43] Favre, A., "Equations des Gaz Turbulents Compressibles," *Journal de Mécanique*, Vol. 4, No. 3, 1965, pp. 361–390.

[44] Knight, D., Zhou, G., Okong'o, N., and Shukla, V., "Compressible Large Eddy Simulation Using Unstructured Grids," AIAA Paper 1998-0535, Jan 1998.

[45] Reynolds, O., "On the Dynamical Theory of Incompressible Viscous Fluids and the Determination of the Criterion," *Philosophical Transactions of the Royal Society of London*, Vol. 186, 1895, pp. 123.

[46] Robinson, D. F. and Hassan, H. A., "Further Development of the k–ζ(Enstrophy) Turbulence Closure Model," *AIAA Journal*, Vol. 36, No. 10, 1998, pp. 1825–1833.

[47] Alexopoulos, G. A. and Hassan, H. A., "A k–ζ(Enstrophy) Model for Mixing Layers and Wall Bounded Flows," AIAA Paper 1996-2039, June 1996.

[48] Robinson, D. F., Harris, J. E., and Hassan, H. A., "Unified Turbulence Closure Model for Axisymmetric and Planar Free Shear Flows," *AIAA Journal*, Vol. 33, No. 12, 1995, pp. 2325–2331.

[49] McDaniel, R. D., Nance, R. P., and Hassan, H. A., "Transition Onset Prediction for High Speed," *Journal of Spacecraft and Rockets*, Vol. 37, No. 3, 2000, pp. 304–309.

[50] Xiao, X., Edwards, J. R., and Hassan, H. A., "Transitional Flow over an Elliptic Cone at Mach 8," *Journal of Spacecraft and Rockets*, Vol. 38, No. 6, 2001, pp. 941–945.

[51] Schetz, J. A., *Boundary Layer Analysis*, Prentice Hall, New Jersey, 1993.

[52] Smits, A. J. and Dussauge, J.-P., *Turbulent Shear Layers in Supersonic Flow*, AIP Press, New York, 1996.

[53] Morkovin, M. V., "Effects of Compressibility in Turbulence Flow," *The Mechanics of Turbulence*, edited by A. Favre, Gordon and Breach, 1962.

[54] Hassan, H. A., "Scaling for the Rescaling-Reintroducing Procedure," unpublished.

[55] Settles, G. S. and Dodson, L. J., "Hypersonic Shock/Boundary-Layer Interaction Database," NASA Contractor Report 177577, April 1991.

[56] Zheltovodov, A. A., Zaulichnii, E. G., Trofimov, V. M., and Yakolev, V. N., "Heat Transfer and Turbulence Study in Compressible Separated Flows," Preprint 22-87, Inst. Theoretical and Applied Mechanics, Russian Acad. of Sciences, Novosobirsk, 1987.

[57] “Advances in Turbulence Modelling,” Lecture Series 1998-05, von Karman Institute for Fluid Dynamics, Belgium, March 1998.

[58] Edwards, J. R., “A Low Diffusion Flux Splitting Scheme for Navier-Stokes Calculations,” *Computers & Fluids*, Vol. 26, No. 6, 1997, pp. 635–659.

[59] Harten, A., “Uniformly High-Order Accurate Nonoscillatory Schemes. I,” *SIAM Journal on Numerical Analysis*, Vol. 24, No. 2, 1987, pp. 279–309.

[60] Reed, M., Private Communication, North Carolina Supercomputing Center.

Appendix A

Numerical Scheme

The governing equations for current LES/RANS hybrid schemes can be expressed in the computational space ξ, η and ς as

$$\frac{1}{J}\frac{\partial \mathbf{U}}{\partial t} + \frac{\partial}{\partial \xi}\left(\mathbf{F} - \mathbf{F}_v\right) + \frac{\partial}{\partial \eta}\left(\mathbf{G} - \mathbf{G}_v\right) + \frac{\partial}{\partial \varsigma}\left(\mathbf{H} - \mathbf{H}_v\right) = \frac{1}{J}\mathbf{S} \tag{A.1}$$

where t is the time, $\mathbf{U}$ the vector of conservative variables, $\mathbf{F}$, $\mathbf{G}$, $\mathbf{H}$ the inviscid flux vectors, $\mathbf{F}_v$, $\mathbf{G}_v$, $\mathbf{H}_v$ the viscous flux vectors, $\mathbf{S}$ the source terms in governing equations and J the Jacobian of the coordinate transformation

$$J = \det \frac{\partial(\xi, \eta, \varsigma)}{\partial(x, y, z)} \tag{A.2}$$

The vector of conservative variables are given by

$$\mathbf{U} = \begin{bmatrix} \bar{\rho} \\ \bar{\rho}\tilde{u} \\ \bar{\rho}\tilde{v} \\ \bar{\rho}\tilde{w} \\ \bar{\rho}\tilde{E} \\ \bar{\rho}k \\ \bar{\rho}\zeta \end{bmatrix} \tag{A.3}$$

and the vector of fluxes

$$\mathbf{F} = \frac{1}{J}\begin{bmatrix} \bar{\rho}\tilde{\mathcal{U}} \\ \bar{\rho}\tilde{u}\tilde{\mathcal{U}} + \xi_x\bar{p} \\ \bar{\rho}\tilde{v}\tilde{\mathcal{U}} + \xi_y\bar{p} \\ \bar{\rho}\tilde{w}\tilde{\mathcal{U}} + \xi_z\bar{p} \\ \bar{\rho}\tilde{H}\tilde{\mathcal{U}} \\ \bar{\rho}k\tilde{\mathcal{U}} \\ \bar{\rho}\zeta\tilde{\mathcal{U}} \end{bmatrix} \tag{A.4}$$

$$\mathbf{G} = \frac{1}{J}\begin{bmatrix} \bar{\rho}\tilde{\mathcal{V}} \\ \bar{\rho}\tilde{u}\tilde{\mathcal{V}} + \eta_x\bar{p} \\ \bar{\rho}\tilde{v}\tilde{\mathcal{V}} + \eta_y\bar{p} \\ \bar{\rho}\tilde{w}\tilde{\mathcal{V}} + \eta_z\bar{p} \\ \bar{\rho}\tilde{H}\tilde{\mathcal{V}} \\ \bar{\rho}k\tilde{\mathcal{V}} \\ \bar{\rho}\zeta\tilde{\mathcal{V}} \end{bmatrix} \tag{A.5}$$

$$\mathbf{H} = \frac{1}{J}\begin{bmatrix} \bar{\rho}\tilde{\mathcal{W}} \\ \bar{\rho}\tilde{u}\tilde{\mathcal{W}} + \varsigma_x\bar{p} \\ \bar{\rho}\tilde{v}\tilde{\mathcal{W}} + \varsigma_y\bar{p} \\ \bar{\rho}\tilde{w}\tilde{\mathcal{W}} + \varsigma_z\bar{p} \\ \bar{\rho}\tilde{H}\tilde{\mathcal{W}} \\ \bar{\rho}k\tilde{\mathcal{W}} \\ \bar{\rho}\zeta\tilde{\mathcal{W}} \end{bmatrix} \tag{A.6}$$

$$\mathbf{F}_v = \frac{1}{J}\begin{bmatrix} 0 \\ \xi_{x_i}(\tilde{\mathcal{T}}_{i1} + \tau_{i1}) \\ \xi_{x_i}(\tilde{\mathcal{T}}_{i2} + \tau_{i2}) \\ \xi_{x_i}(\tilde{\mathcal{T}}_{i3} + \tau_{i3}) \\ \xi_{x_i}[\tilde{u}_j(\tilde{\mathcal{T}}_{ij} + \tau_{ij}) - \tilde{q}_i - Q_i] \\ \xi_{x_i}\left(\frac{\mu}{3} + \frac{\mu_t}{\sigma_k}\right)\frac{\partial k}{\partial x_i} \\ \xi_{x_i}\left(\mu + \frac{\mu_t}{\sigma_\zeta}\right)\frac{\partial \zeta}{\partial x_i} \end{bmatrix} \tag{A.7}$$

$$\mathbf{G}_v = \frac{1}{J}\begin{bmatrix} 0 \\ \eta_{x_i}(\tilde{\mathcal{T}}_{i1}+\tau_{i1}) \\ \eta_{x_i}(\tilde{\mathcal{T}}_{i2}+\tau_{i2}) \\ \eta_{x_i}(\tilde{\mathcal{T}}_{i3}+\tau_{i3}) \\ \eta_{x_i}[\tilde{u}_j(\tilde{\mathcal{T}}_{ij}+\tau_{ij})-\tilde{q}_i-Q_i] \\ \eta_{x_i}\left(\frac{\mu}{3}+\frac{\mu_t}{\sigma_k}\right)\frac{\partial k}{\partial x_i} \\ \eta_{x_i}\left(\mu+\frac{\mu_t}{\sigma_\zeta}\right)\frac{\partial \zeta}{\partial x_i} \end{bmatrix} \tag{A.8}$$

$$\mathbf{H}_v = \frac{1}{J}\begin{bmatrix} 0 \\ \varsigma_{x_i}(\tilde{\mathcal{T}}_{i1}+\tau_{i1}) \\ \varsigma_{x_i}(\tilde{\mathcal{T}}_{i2}+\tau_{i2}) \\ \varsigma_{x_i}(\tilde{\mathcal{T}}_{i3}+\tau_{i3}) \\ \varsigma_{x_i}[\tilde{u}_j(\tilde{\mathcal{T}}_{ij}+\tau_{ij})-\tilde{q}_i-Q_i] \\ \varsigma_{x_i}\left(\frac{\mu}{3}+\frac{\mu_t}{\sigma_k}\right)\frac{\partial k}{\partial x_i} \\ \varsigma_{x_i}\left(\mu+\frac{\mu_t}{\sigma_\zeta}\right)\frac{\partial \zeta}{\partial x_i} \end{bmatrix} \tag{A.9}$$

where

$$\mathcal{U} = \xi_{x_i}\tilde{u}_i \tag{A.10}$$

$$\mathcal{V} = \eta_{x_i}\tilde{u}_i \tag{A.11}$$

$$\mathcal{W} = \varsigma_{x_i}\tilde{u}_i \tag{A.12}$$

The second-order-accurate time integration of equation(A.1) was obtained by implicit

planar ILU subiterations, which may be represented as follows

$$\begin{aligned} & \mathbf{D}\Delta\mathbf{W}^{(n)}_{i,j,k} + \mathbf{A}^{+}\Delta\mathbf{W}^{(n)}_{i+1,j,k} + \mathbf{A}^{-}\Delta\mathbf{W}^{(n)}_{i-1,j,k} + \\ & \mathbf{B}^{+}\Delta\mathbf{W}^{(n)}_{i,j+1,k} + \mathbf{B}^{-}\Delta\mathbf{W}^{(n)}_{i,j-1,k} + \\ & \mathbf{C}^{+}\Delta\mathbf{W}^{(n)}_{i,j,k+1} + \mathbf{C}^{-}\Delta\mathbf{W}^{(n)}_{i,j,k-1} \\ = \quad & \frac{1}{\Delta t J}(\mathbf{U}^{(n-1)} - \mathbf{U}^{N}) + \frac{1}{2}(\mathbf{R}^{(n-1)} + \mathbf{R}^{N}) \end{aligned} \tag{A.13}$$

where i, j, and k are the indices of a gird cell, $\mathbf{W}$ is the vector of primitive variables

$$\mathbf{W} = \begin{bmatrix} \bar{\rho} \\ \tilde{u} \\ \tilde{v} \\ \tilde{w} \\ \tilde{T} \\ k \\ \zeta \end{bmatrix} \tag{A.14}$$

and

$$\mathbf{W}^{(0)} = \mathbf{W}^{N} \tag{A.15}$$

$$\mathbf{W}^{(n)} = \mathbf{W}^{(n-1)} + \Delta\mathbf{W}^{(n-1)}, \quad n = 1, 2, \cdots \tag{A.16}$$

$\mathbf{W}^{N}$ is the $\mathbf{W}$ at the N time level, and $\mathbf{W}^{(n)}$ is the result after n subiterations, which will converge to $\mathbf{W}^{N+1}$.

$\mathbf{R}$ is the summation of the fluxes, which is defined by

$$\begin{aligned}\mathbf{R} &= \mathbf{F}_{i+\frac{1}{2},j,k} - \mathbf{F}_{i-\frac{1}{2},j,k} - \left(\mathbf{F}_{v,i+\frac{1}{2},j,k} - \mathbf{F}_{v,i-\frac{1}{2},j,k}\right) + \\ &\quad \mathbf{G}_{i,j+\frac{1}{2},k} - \mathbf{G}_{i,j-\frac{1}{2},k} - \left(\mathbf{G}_{v,i,j+\frac{1}{2},k} - \mathbf{G}_{v,i,j-\frac{1}{2},k}\right) + \\ &\quad \mathbf{H}_{i,j,k+\frac{1}{2}} - \mathbf{H}_{i,j,k-\frac{1}{2}} - \left(\mathbf{H}_{v,i,j,k+\frac{1}{2}} - \mathbf{H}_{v,i,j,k-\frac{1}{2}}\right) + \\ &\quad \frac{1}{J}\mathbf{S}_{i,j,k} \end{aligned} \tag{A.17}$$

where $\mathbf{A}^{\pm}$, $\mathbf{B}^{\pm}$, $\mathbf{C}^{\pm}$ and $\mathbf{D}$ are the coefficient matrices

$$\mathbf{D} = \frac{\partial \mathbf{R}}{\partial \mathbf{W}}_{i,j,k} + \frac{1}{J}(\frac{1}{\tau} + \frac{1}{\Delta t}) \tag{A.18}$$

$$\mathbf{A}^{\pm} = \frac{\partial \mathbf{R}}{\partial \mathbf{W}}_{i\pm1,j,k} \tag{A.19}$$

$$\mathbf{B}^{\pm} = \frac{\partial \mathbf{R}}{\partial \mathbf{W}}_{i,j\pm1,k} \tag{A.20}$$

$$\mathbf{C}^{\pm} = \frac{\partial \mathbf{R}}{\partial \mathbf{W}}_{i,j,k\pm1} \tag{A.21}$$

τ is the pseudo time step, while Δt is the physical time step.

A planar Gauss-Seidel method is used to solved equation(A.13), which consists of backward sweep and forward sweep in ξ (or i) direction:

Step 1 backward sweep in ξ direction

$$\begin{aligned}\mathbf{D}_i^{(n)}\Delta\mathbf{W}_i^{(n+\frac{1}{2})} &= \omega_b\left[\mathcal{R}(\mathbf{W}_i^{(n)}) - \mathbf{A}^{+}\Delta\mathbf{W}_{i+1}^{(n+\frac{1}{2})}\right] \\ \mathbf{W}_i^{(n+\frac{1}{2})} &= \mathbf{W}_i^{(n)} + \Delta\mathbf{W}_i^{(n+\frac{1}{2})}\end{aligned} \tag{A.22}$$

Step 2 forward sweep in ξ direction

$$\mathbf{D}_i^{(n+\frac{1}{2})}\Delta\mathbf{W}_i^{(n)} = \omega_f\left[\mathcal{R}(\mathbf{W}_i^{(n+\frac{1}{2})}) - \mathbf{A}^{-}\Delta\mathbf{W}_{i-1}^{(n+1)}\right] \tag{A.23}$$

$$\mathbf{W}_i^{(n+1)} = \mathbf{W}_i^{(n+\frac{1}{2})} + \Delta\mathbf{W}_i^{(n+1)} \tag{A.24}$$

Here, ω_b and ω_f are under-relaxation coefficients, subscript i indicates the operations and variables in a i-plane, $\mathcal{R}(\mathcal{W}^{(n-1)})$ is the RHS of equation(A.13) and $\mathbf{D}_i\Delta\mathbf{W}_i^{(n)}$ stands for

$$\begin{aligned}\mathbf{D}_i\Delta\mathbf{W}_i^{(n)} &= \mathbf{D}\Delta\mathbf{W}_{i,j,k}^{(n)} + \mathbf{B}^+\Delta\mathbf{W}_{i,j+1,k}^{(n)} + \mathbf{B}^-\Delta\mathbf{W}_{i,j-1,k}^{(n)} + \\ &\quad \mathbf{C}^+\Delta\mathbf{W}_{i,j,k+1}^{(n)} + \mathbf{C}^-\Delta\mathbf{W}_{i,j,k-1}^{(n)} \end{aligned} \tag{A.25}$$

To solve (A.22) and (A.23), coefficient matrix $\mathbf{D}_i$ was factorized using incomplete-LU (ILU) factorization.

To achieve second-order accuracy in spatial directions, LDFSS[58] and second-order ENO scheme[59] were used to calculate inviscid fluxes, and the derivatives in viscous fluxes were discretized using central differences.

Appendix B

Speedup Test of Parallel Code

The code used in this work was originally developed by Dr. J. R. Edwards. It was parallelized using Message Passing Interface (MPI) and optimized for the IBM SP3 parallel machine. The data communication module of this code was modified by current author using non-blocking message passing.

The speedup test was conducted in the LES/RANS inflow generation computation. The grid size for this problem is $129 \times 129 \times 65$. The computation domain was decomposed into 32, 64 and 128 blocks, respectively, as presented in Table.B.1. To get load-balancing, each block had the same size and was mapped into one processor, respectively. Because of the planar ILU scheme, which requires large size of memory, the code cannot run in 8 or 16 blocks.

Table B.1: The decomposition of the whole domain

# of blocks	Decomposition Scheme	# of grid nodes in each block
32	$8 \times 4 \times 1$	$17 \times 33 \times 65$
64	$8 \times 4 \times 2$	$17 \times 33 \times 33$
128	$8 \times 8 \times 2$	$17 \times 17 \times 33$

In each test, the code started timing right before it entered the main loop of iterations and stopped timing after it finished 250 main iterations. The time consumed in the initialization of computations was not considered. The number of subiterations was set to be

always 4 in the test. The non-blocking communication scheme was used for the message passing between adjacent blocks. In order to get stable timing results, the code was running in the mode of 4-process-per-node. The test results are shown in Table B.2 and Figure B.1. The "speedup" in Table B.2 is defined as

$$speedup = \frac{t_{w,32}}{t_{w,N}} \tag{B.1}$$

Table B.2: The Results of Speedup Test

# of processors, N	wall clock time(sec), t_w	# of iteration/sec	Speedup
32	3325	75.19×10^{-3}	1.00
64	1527	163.72×10^{-3}	2.18
128	764	327.22×10^{-3}	4.35

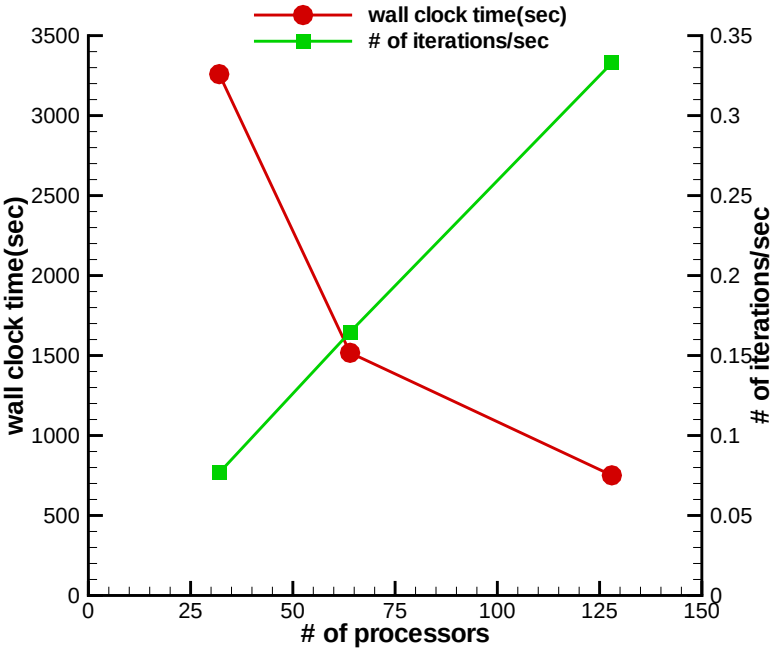

Figure B.1: Speedup Results

Note that the *speedup* of 64- and 128-block cases are better than the theoretical 2 and

Table B.3: L2 usage and the communication time

# of processors, N	# of loads per L2 miss	$\frac{\text{communication time(processor 0)}}{\text{wall clock time}}$
32	1137.38	195/3325
64	1425.15	106/1527
128	3566.10	93/764

4, respectively. Thus, we got the *superlinear* speedup. Under the current hardware environment, it can be explained as follows[60].

The superlinear speedup is mainly due to cache effects. On RISC(like SP[1]) processors, the chip performance is largely determined by getting good cache reuse. As the program is spread over more processors, the more of code is running out of cache. Table B.3 lists the L2 usage and the communication time for the three cases. As the number of blocks increases, the the efficiency of L2 cache increases. For the 128-block case, the L2 cache reuse increases so much that it offsets the communication losses.

[1]Each processor on the SP Power3 has 8 MB of L2 cache